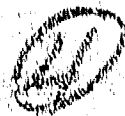


DTIC FILE COPY



Technical Report 1081

A Systems Approach to the Torque Control of a Permanent Magnet Brushless Motor

AD-A209 395

Benjamin J. Paul

MIT Artificial Intelligence Laboratory

NOT REPRODUCIBLE BY OTHERS
FOR OFFICIAL USE ONLY
UNLESS INDICATED OTHERWISE

DTIC
ELECTE
JUN 23 1989
S E D

83 G 29 018

UNCLASSIFIED

SECURITY CLASSIFICATION OF THIS PAGE (When Data Entered)

REPORT DOCUMENTATION PAGE		READ INSTRUCTIONS BEFORE COMPLETING FORM
1. REPORT NUMBER AI TR 1081	2. GOVT ACCESSION NO.	3. RECIPIENT'S CATALOG NUMBER
4. TITLE (and Subtitle) A Systems Approach to the Torque Control of a Permanent Magnet Brushless Motor		5. TYPE OF REPORT & PERIOD COVERED technical report
		6. PERFORMING ORG. REPORT NUMBER
7. AUTHOR(s) Benjamin J. Paul		8. CONTRACT OR GRANT NUMBER(s) N00014-86-K-0085 -N00014-85-K-0124
9. PERFORMING ORGANIZATION NAME AND ADDRESS Artificial Intelligence Laboratory 545 Technology Square Cambridge, MA 02139		10. PROGRAM ELEMENT, PROJECT, TASK AREA & WORK UNIT NUMBERS
11. CONTROLLING OFFICE NAME AND ADDRESS Advanced Research Projects Agency 1400 Wilson Blvd. Arlington, VA 22209		12. REPORT DATE August 1987
		13. NUMBER OF PAGES
14. MONITORING AGENCY NAME & ADDRESS (if different from Controlling Office) Office of Naval Research Information Systems Arlington, VA 22217		15. SECURITY CLASS. (of this report) UNCLASSIFIED
		15a. DECLASSIFICATION/DOWNGRADING SCHEDULE
16. DISTRIBUTION STATEMENT (of this Report) Distribution is unlimited		
17. DISTRIBUTION STATEMENT (of the abstract entered in Block 20, if different from Report) Unlimited		
18. SUPPLEMENTARY NOTES None		
19. KEY WORDS (Continue on reverse side if necessary and identify by block number) Torque Ripple Brushless		
20. ABSTRACT (Continue on reverse side if necessary and identify by block number) See Back of Page		

DD FORM 1473
1 JAN 73EDITION OF 1 NOV 68 IS OBSOLETE
S/N 0102-014-6601

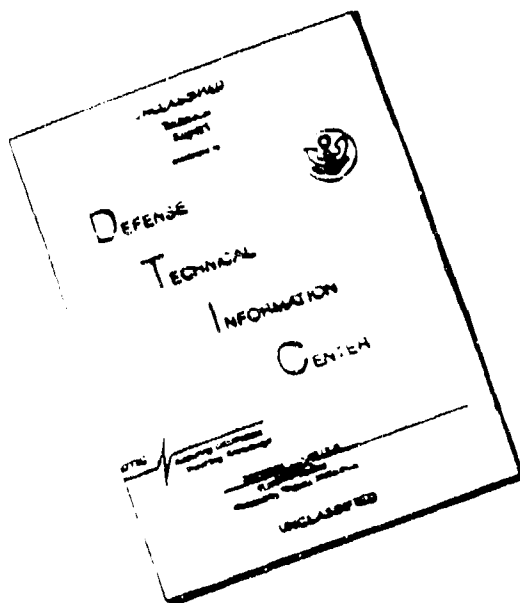
UNCLASSIFIED

SECURITY CLASSIFICATION OF THIS PAGE (When Data Entered)

Block 20 cont'd

Many approaches to force control have assumed the ability to command torques accurately. Concurrently, much research has been devoted to developing accurate torque actuation schemes. Often, torque sensors have been utilized to close a feedback loop around output torque. In this paper, the torque control of a brushless motor is investigated through: the design, construction, and utilization of a joint torque sensor for feedback control; and the development and implementation of techniques for phase current based feedforward torque control. It is concluded that simply closing a torque loop is no longer necessarily the best alternative since reasonably accurate current based torque control is achievable.

DISCLAIMER NOTICE



THIS DOCUMENT IS BEST
QUALITY AVAILABLE. THE COPY
FURNISHED TO DTIC CONTAINED
A SIGNIFICANT NUMBER OF
PAGES WHICH DO NOT
REPRODUCE LEGIBLY.

**A Systems Approach
to the Torque Control of a
Permanent Magnet Brushless Motor**

by

Benjamin J. Paul

B.S. Mechanical Engineering
Worcester Polytechnic Institute
(1985)

*Submitted to the Department
of Mechanical Engineering
in Partial Fulfillment of
the Requirements for the
Degree of*

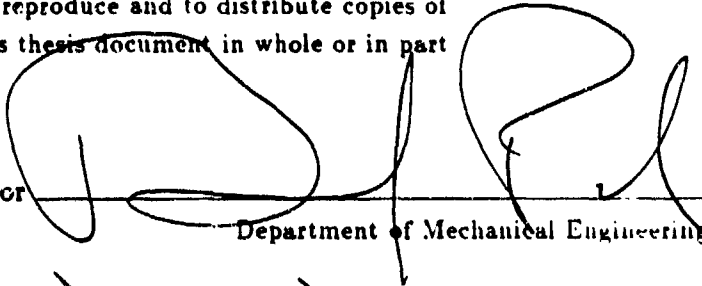
Master of Science in
Mechanical Engineering
at the

MASSACHUSETTS INSTITUTE OF TECHNOLOGY
August 1987

© Benjamin J. Paul

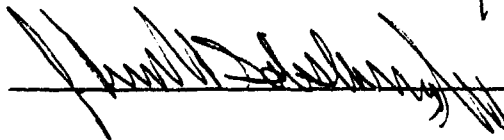
The author hereby grants to MIT permission
to reproduce and to distribute copies of
this thesis document in whole or in part

Signature of Author



Department of Mechanical Engineering

Certified by



Ken Salisbury
Thesis Supervisor

Accepted by

Ain Souin
Department Head

**A Systems Approach
to the Torque Control of a
Permanent Magnet Brushless Motor**

by

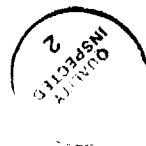
Benjamin J. Paul

Submitted to the Department of Mechanical Engineering
on August 7, 1987 in Partial Fulfillment of the
Requirements for the Degree of Master of Science in
Mechanical Engineering

Abstract

Many approaches to force control have assumed the ability to command torques accurately. Concurrently, much research has been devoted to developing accurate torque actuation schemes. Often, torque sensors have been utilized to close a feedback loop around output torque. In this paper, the torque control of a brushless motor is investigated through: the design, construction, and utilization of a joint torque sensor for feedback control; and the development and implementation of techniques for phase current based feedforward torque control. It is concluded that simply closing a torque loop is no longer necessarily the best alternative since reasonably accurate current based torque control is achievable.

Thesis Supervisor: Dr. Kenneth Salisbury



Author	
Title	
Department	
Date	
Checked by	
Checked date	
Checked by	
Checked date	
Checked by	
Checked date	

A-1

Acknowledgements

Many individuals provided assistance and support for my thesis research and I would like to offer my thanks. First, I would like to express my appreciation to the entire AI Lab community. Time spent on my thesis has been extremely enjoyable and this is due in most part to the many relationships developed with people at the lab. In particular, Ron Wiken was invaluable in his efforts to procure hardware and supplies. The members of the Mobot Group were particularly tolerant and continued to offer advice, equipment, and their time despite my incessant and verbose intrusions. I would also like to thank Brian Eberman. His enthusiasm provided the extra push that I needed to finish this thesis. Thanks go to my sister, Dr. Elizabeth Lofton, who attempted to keep her little brother apprised of deadlines throughout graduate school. My parents, as they have always done, provided the love and support that everyone should have. I would like to thank the Office of Naval Research for their financial support and the staff of the American Society of Engineering Education for their efforts in administering ONR funds in a very professional and helpful manner. Finally, I would like to thank my advisor Dr. Kenneth Salisbury, a particularly intelligent, super individual, who stands out as a researcher, advisor, and a friend.

This report describes research done at the Artificial Intelligence Laboratory of the Massachusetts Institute of Technology. Support for the laboratory's artificial intelligence research is provided in part by the Office of Naval Research University Research Initiative Program under Office of Naval Research contract N00014-86-K-0685 and in part by the Advanced Research Projects Agency of the Department of Defense under Office of Naval Research contract N00014-85-K-0124.

Table of Contents

1	Introduction	7
1.1	Background	7
1.2	Research in Force Control	9
2	Brushless Motors and Controllers	16
2.1	Brushless Motors	16
2.2	Brushless Motor Controllers	18
2.3	Moog Brushless Motor and Torque Controller	20
3	Torque Control	23
3.1	The Need for Torque Control	23
3.2	Torque Measurement	26
3.3	Development of a Joint Torque Sensor	31
3.4	Signal Noise Reduction	39
4	Current Base Torque Control	42
4.1	Torque Inference from Phase Currents	42
4.2	Sources of Torque Ripple	43
4.3	Torque Ripple Compensation	56
5	Results	59
5.1	Torque Sensor Results	59
5.2	Current Based Torque Control Results	67
6	Conclusions	79
	Appendices	79
	Appendix I: Moog Equipment	81
	Appendix II: Cantilever Sensor	85
	Appendix III: Joint Torque Sensor	88
	References	93

List of Figures

2.1	Brushless Motor Controller Configuration	19
2.2	Moog Controller and Power Supply	22
3.1	Cantilever Torque Sensor	29
3.2	Output Pulley Cable Drive	32
3.3	Joint Torque Sensor	33
3.4	Joint Torque Sensor Schematic	34
3.5	Sensing Element Schematic	35
3.6	Sensing Element Exploded View	35
3.7	Strain Gauge Layout	36
3.8	Joint Torque Sensor Electronics	38
3.9	Joint Torque Sensor on Cable Drive	39
3.10	Shielding Schematic	41
4.1	Moog Motor Torque Ripple Characteristics	45
4.2	8 θ Ripple Component	49
4.3	4 θ Ripple Component	51
4.4	Deadband Torque Ripple	52
4.5	Harmonic Induced Ripple	54
5.1	Torque Sensor Calibration	62
5.2	1Hz Output	63
5.3	5Hz Output	63
5.4	10Hz Output	64
5.5	25Hz Output	64
5.6	50Hz Output	65
5.7	Low Frequency Zero Response	65
5.8	Schematic of Components	66
5.9	High Frequency Zero Response	66
5.10	Schematic of Components	67
5.11	Moog Controller Calibration Curve	69
5.12	Torque-Loop-Closure Based Compensation	70
5.13	Feedforward Current Based Torque Control	72
5.14	Harmonic Identification Data	74
5.15	Motor Spacial Harmonics	75
5.16	Harmonic Ripple	77
5.17	Harmonic Ripple Compensation	78

A.1.1 Moog 303-003 Motor 83

A.1.2 Moog 303-003 Performance Curve 84

A.2.1 Cantilever Sensor 86

A.2.2 Cantilever Electronics 87

A.3.1 Joint Sensor Electronics 91

Chapter 1

Introduction

1.1 Background

A significant portion of the research conducted at MIT's Artificial Intelligence Lab is devoted to robotics. In our group, headed by Dr. Ken Salisbury, research is being conducted on the design and control of robotic arms and manipulators. One aspect of the work centers around the Salisbury Hand, including the development of control strategies, grasp planning techniques, and sensor development and implementation. More recently, the scope of research has expanded to include development of a low friction cable driven manipulator.

When my research began, my job was to investigate permanent magnet brushless DC motor technology. The lab's interest was fourfold: First, permanent magnet brushless DC motor and controller technology was improving rapidly. Second, it appeared that permanent magnet brushless DC motors, hereafter referred to as brushless motors, would find broad application in the robotic field as performance specifications improved and unit prices dropped. Third, brushless motors represented a logical evolution of the technology used in the conventional DC brush motors on the Salisbury Hand. Finally, the use of brushless motors promised to eliminate the large brush friction characteristic of conventional motors and to improve torque and response characteristics. Given the

lab's interest. the goal of my thesis research became to select a brushless motor and controller for the lab, study and develop techniques for brushless motor torque control, and evaluate the usefulness of brushless motors in force control applications.

I felt that the best approach to accomplishing all or part of this goal would be to take a systems approach. By this, I mean that it is important to look at all parts of a torque control system and make improvements in those areas which will most effectively increase the accuracy of the system as a whole. I felt that it was important not to optimize one piece of the system without first determining where improvements could be made and whether any parts of the system were redundant. For example, I sought to answer the question, are mechanical torque sensors necessary for accurate torque control?

During my research, experimental work was carried out using a brushless motor and torque controller purchased from Moog Inc. The Moog equipment was chosen for several reasons after surveying the brushless motors and controllers available commercially: 1) the motor/controller exhibited good performance characteristics in the range we were interested in, 2) the controller was designed for sinusoidal commutation, 3) the controller allowed us to get hooks into areas that we were interested in, and 4) the Moog documentation appeared to be clear and complete. In my research, first a mechanically compliant torque sensor was developed to allow torque feedback and closed loop torque control. The torque sensor was designed to be compatible with the new cable driven manipulator design being developed by the lab. In the second, the torque

characteristics of the motor were investigated. Then, two methods were developed to accurately control motor output torque. In the first method, feedforward open loop compensation techniques, utilizing closed loop phase current control, were implemented to minimize torque ripple.

The next section outlines the major research that has been done in force control. Chapter 2 presents a brief description of brushless motors, their performance characteristics, and control. In addition, a description is given of the Moog brushless motor and controller used in this research. Chapter 3 discusses the need for accurate torque control, citing relevant research. The development of torque sensors to improve torque control characteristics is then presented. In Chapter 4, various sources of brushless motor torque ripple are described and methods are given for minimizing torque ripple based on current waveform modification and feedforward compensation. In the final chapter, results of the two torque control techniques are compared and critiqued.

1.2 Research in Force Control

Research in force control has been aimed at developing accurate methods to control the interaction forces between a robotic manipulator and its environment. Many researchers have cited the need to control contact forces while executing certain tasks. Ideally, one desires a practically limitless bandwidth mechanism that can apply commanded forces and control interaction forces resulting from contact with an uncertain environment. This usually implies that one can command manipulator position along

some axes of motion in addition to interaction force along orthogonal axes.

In order to put force control research into perspective, it is necessary to review the work that has been done. Whitney (1985) provided a good overview of force control strategies. Maples (1986) followed with a framework to categorize force control implementations. In view of these I will present an overview of the basic approaches to force control and then give a more or less chronological listing of force control research in order to better convey the current state of force control research and where it is headed.

Manipulator force control techniques can be either passive, active or both. Passively compliant manipulators can be designed to exhibit compliance in certain directions in order to control contact forces. Drake's (1978) Remote Centered Compliance, developed at Draper Labs, is perhaps the best known passively compliant force control implementation. Active force control involves controlling forces through actuator commands. In open loop or implicit force control, there is no force feedback. Contact forces are controlled by commanding joint torques or adjusting servo gains to achieve a desired manipulator stiffness. Force control implementations on the Direct Drive Arm (An 1986) are a good example. There are four other types of active force control which involve some type of feedback.

The first type, referred to as damping (Whitney 1977), accommodation, or admittance control, transforms sensed forces into joint velocity commands through application of a so-called inverse damping matrix. Damping control can be achieved without

invoking an inverse damping matrix, by adjusting the velocity feedback gains at the joints (Abramowitz 1984). It is arguable that this falls into the category of passive force control. Stiffness control (Salisbury 1980), the second type of active feedback force control techniques, specifies a linear relationship between position error and commanded force. Sensed forces are transformed into commanded positions. The third type, impedance control (Hogan 1985), utilizes damping and stiffness matrices to control the relationship between the deviation from the commanded virtual manipulator position and the forces exerted by the manipulator on the environment. Stiffness control could be considered a subset of impedance control. Finally, hybrid force/position control (Raibert and Craig), involves using two complementary control systems. Position and force control loops operate simultaneously to control interactions with the environment.

In order to better understand these techniques, it is necessary to look at the details of their implementation. It is also useful to put them in better context with other work in force control. Inoue (1974) demonstrated that precise assembly could be achieved with a robot employing feedback from a force sensing wrist. The first attempt at hybrid active force control involved a Cartesian based force control scheme. The goal of this hybrid technique was to simultaneously satisfy orthogonal position and force trajectory constraints in Cartesian space. Paul and Shimano (1976) implemented a Cartesian based force specification in manipulator joint space. In their work, joints most nearly aligned with compliant specifications in Cartesian space were controlled

to provide force, while the remaining joints were position controlled. Motor currents were measured to infer joint torque. Shimano and Roth (1976) presented a paper on force sensing. Their work included a technique for the automatic calibration of a wrist force sensor. Whitney proposed the "generalized damper" force control scheme in (1977) in which force sensor feedback was transformed to joint velocity commands with an inverse damping matrix. Whitney proposed that a stable inverse damping matrix could be formulated with knowledge of the combined stiffness of the environment and force sensor. Whitney's implementation used a wrist mounted force/torque sensor.

Salisbury (1980) developed stiffness control, a new approach to implementing Cartesian based active force control. In Salisbury's approach, a Cartesian stiffness matrix is transformed into joint space, permitting rapid routine computation. Salisbury's method yields a joint stiffness matrix from a specified Cartesian stiffness matrix by premultiplying by the Jacobian transpose and postmultiplying by the Jacobian. Unlike the approximate method of Paul and Shimano (1976), joints are driven to achieve a desired Cartesian stiffness and are not dedicated to either force or position control.

Wu and Paul (1980) developed and implemented a joint torque sensor for a single joint manipulator. The feedback loop was closed around the joint's gear reduction unit. The analog control system used was capable of high gain and bandwidth although the stability problem was not analyzed. Wu and Paul argued that good force sensing techniques are imperative to accurate force control and that sensed torque is more readily integrated into a control scheme than wrist sensor force data.

Mason (1981) presented a theoretical analysis of force control in Cartesian space based on natural and artificial constraints. Natural force and position constraints are imposed by the task environment and determine which axis can be force controlled and which can be position controlled. Artificial constraints specify force and position trajectories consistent with natural constraints.

Raibert and Craig (1981) implemented another approach to compliant manipulator control. Force and position errors specified in a Cartesian system were transformed into joint coordinates, multiplied by the joint gain matrix and used to command force and torque at the joints. Cartesian force and position errors were computed based on force sensing wrist and joint position sensor feedback. It is important to note that while each Cartesian degree of freedom was either position controlled or force controlled, actuator torque commands were derived from superposition of both the force and position control loops.

Luh, Fisher, and Paul (1983) implemented closed loop torque servos at the joints of the Stanford Manipulator. The feedback was utilized to reduce frictional effects in the joints and harmonic drive. Stability is discussed and a phase-lead compensator is used to eliminate limit cycles while reducing friction torque. The research addressed the practical need to reduce frictional effects in manipulator joints and drives.

Cannon and Rosenthal (1984) began the investigation of manipulator control with non-colocated actuators and sensors. They contended that with colocation, good stable control is easy to achieve, but that with non-colocated sensors and actuators, it is much

more difficult, especially if the system is flexible and has little damping. The researchers found that in a noncolocated system, "pole zero flipping" occurred as parameters varied.

Paul (1985) outlined a scheme for hybrid control of robotic manipulators in which the constraint surface is mapped to joint axes. Force sensing elements are used and some joints are torque controlled while others are position controlled.

In [85] Whitney reviewed the major force control strategies. He included stiffness control, damping/accomodation, impedance control, explicit force control, hybrid control, and implicit force control in his review. He analyzed stability and concluded that low force feedback gain is required when dealing with high environmental stiffness.

Cannon, Tilley, and Kraft (1986) investigated end point force control of a flexible manipulator with non-colocated sensors and a fast end effector. The wrist subsystem utilized endpoint force feedback to close its own loop on contact force. The wrist force controller treats movement of the main link as a disturbance and greatly improves the end point response of the flexible main manipulator.

Roberts, Paul, and Hillberry (1986) looked at the effect of end effector mechanical stiffness on manipulator control. They concluded that there existed an inherent tradeoff between wrist sensor stiffness and manipulator response for position and force control. A sensor deflection compensator was described which allowed the manipulator to exhibit the same stiffness with a compliant end effector as it would have without the end effector.

Chae An (1986) studied force control of the MIT Direct Drive Arm (DDArm) and

addressed kinematic and dynamic instabilities in robot force control. An presented parameter estimation techniques and computed and feedforward torque control techniques. He described stability problems associated with stiff environment contact as a dynamic stability problem and outlined a kinematic stability problem associated with Raibert and Craig's (1981) hybrid control. An contended that the hybrid control technique of Raibert and Craig does not allow one to kinematically decouple the system eigenvalues. For revolute robots, the eigenvalues are tied to position and therefore cannot be guaranteed to remain stable.

Eppinger and Seering [86] developed a dynamic model of robot force control with force sensor feedback. In modeling some effects of workpiece dynamics and manipulator and sensor stiffness, they concluded that force-controlled instabilities may result from the first mode of the manipulator. In following work (1987), they continued to study manipulator instability and non-colocation. They concluded that dynamics between the actuator and force sensor lead to instabilities when the force loop is closed. In addition, they pointed out that actuator lag and low pass filtering limit closed loop bandwidth and lead to instabilities.

Chapter 2

Brushless Motors and Controllers

2.1 Brushless Motors

Brushless motors, defined for this research as electronically commutated permanent magnet DC motors, are an outgrowth of conventional DC motor technology. In DC motors, the interaction of permanent magnet induced magnetic flux and phase winding current vectors produce torque. Conventional DC motors are constructed with permanent magnets on the stator, phase windings on the rotor, and internal commutation brushes to mechanically switch motor current. The commutation brushes effectively maintain a stationary rotor current field, properly aligned with the stator magnetic field, irrespective of rotor position.

In brushless motors, phase windings are located on the stator and permanent magnets are located on the rotor. Current switching is controlled by electronic commutation circuitry external to the motor. Rotor position is fed back to the motor controller from a resolver, an encoder, or hall effect transducers. Electronic commutation spacially orients the stator phase currents with the rotor field. The stator current field is rotated

to follow the rotor. In order to achieve this, forms of commutation range from simply turning phases on or off based on rotor position feedback to continuously varying phase currents as the motor turns.

Brushless motors have many advantages over conventional DC motors. First, the absence of brushes greatly reduces mechanical friction. Second, higher winding currents can be used without the arcing problems associated with the brushes of conventional motors. Third, replacing rotor coils with high performance magnets reduces rotor inertia and provides improved acceleration and dynamic performance. Finally, the inverted construction of a brushless motor allows heat generated from winding losses to be efficiently removed through the stator. Normally, copper losses are the major cause of heating in the motor. Temperature rises limit the load that a motor can drive because winding insulation normally breaks down at about 155° Celsius. In brushless motors, due to efficient heat dissipation via conduction, winding currents are less limited by restrictions on maximum winding temperature. Conventional DC motors, on the other hand, are restricted to lower winding currents because heat must be dissipated from the rotor by convection alone.

In addition to benefits accruing from their basic design, brushless motors offer several advantages stemming from use of Pulse Width Modulation (PWM) techniques and modern rare earth magnetic materials. PWM allows brushless motors to be driven extremely efficiently. With PWM, phase winding currents are continuously varied by switching the power transistors on and off at high frequency. The motor phases see

an average voltage that is a function of the duty cycle, or percentage of time that the transistors are on. PWM results in high efficiencies because the power transistors are always full on or full off.

Rare earth magnets, in particular Samarium Cobalt magnets, allow higher torque ratings and more nearly linear torque response. The increased torque ratings arise from the extremely high energy product of materials like Samarium Cobalt. Samarium Cobalt's high coercivity lends itself to high field strengths. The torque response is more linear because Samarium Cobalt has a relatively low reversible temperature coefficient (approximately -0.04 %) and a high resistance to the temporary demagnetization effects of armature reaction. The reversible temperature coefficient is a measure of the drop in magnetic field flux strength as a function of temperature. Armature reaction demagnetization is a reversible process in which the motor magnets are demagnetized due to the interaction with the magnetomotive force (MMF) induced by the stator windings.

2.2 Brushless Motor Controllers

Brushless motor controllers contain the electronics to commutate brushless motors. In addition, circuitry can be included to control velocity, torque, or position. Figure 3.1 illustrates the various components and structure of a generalized brushless motor controller.

The controller is provided with position feedback from a shaft mounted brushless

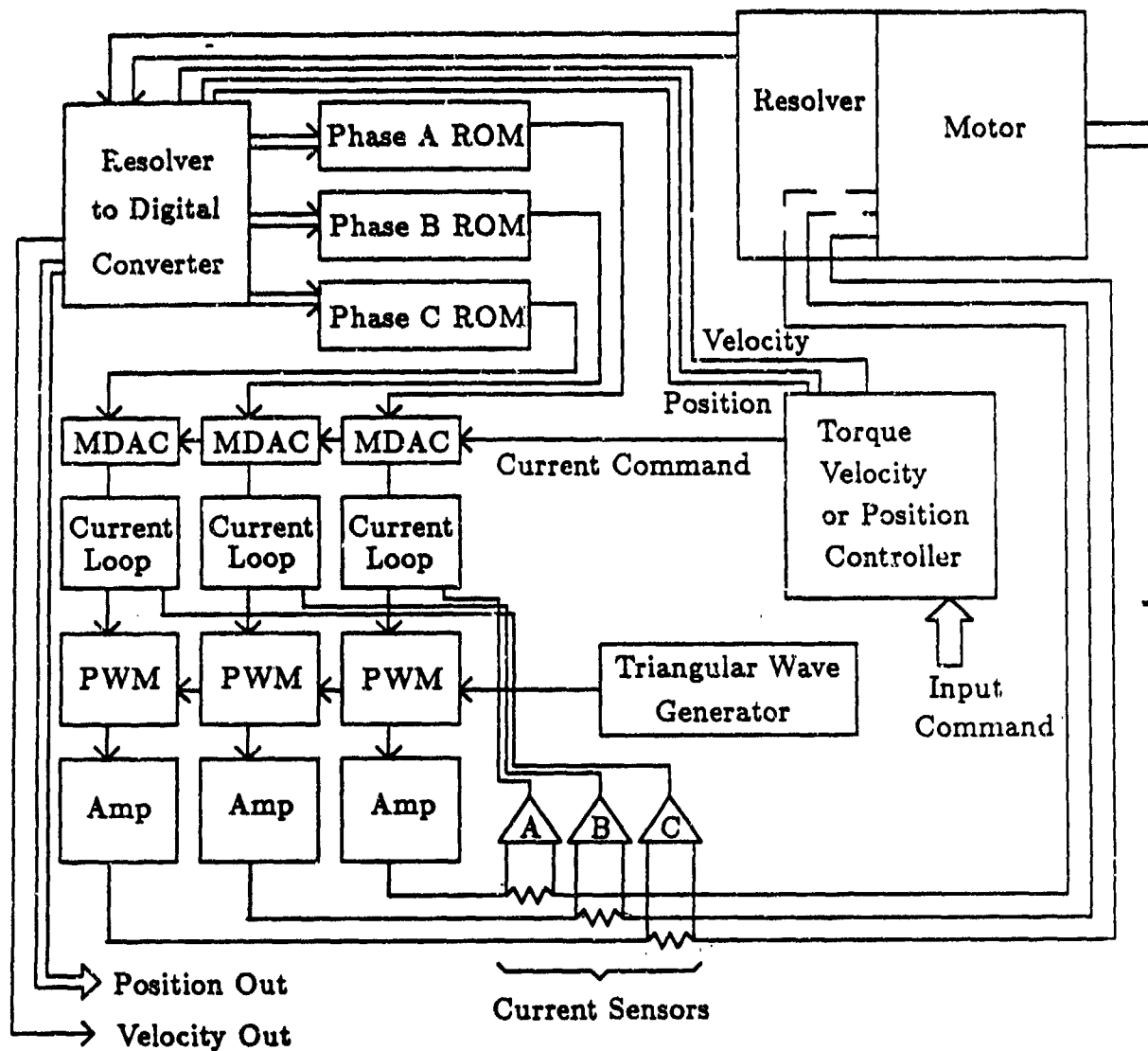


Figure 2.1. A common brushless motor controller configuration.

resolver. The resolver output is converted to a digital shaft angle and used to select relative phase current magnitudes in lookup tables. The values from the lookup table are scaled by the current command and given to the current control loops for each phase. The current command is proportional to desired torque. In a torque controller,

the desired torque is the input to the controller. In a velocity controller, the torque command is calculated by the velocity control loop, based on the desired and actual velocity.

The ROM lookup tables provide the shape of the commutated phase current waveform. In a sinusoidal commutation scheme, the tables contain sinewaves corresponding to the spatial harmonics of the motor. The tables allow one to modify the phase current profiles to modify motor/controller performance.

The current control loop senses the phase current with inline resistors or hall effect devices. The sensed value is compared with the the desired value output by the Multiplying Digital to Analog Converters (MDACs). The current loop controls the PWM of the power stage in order to acheive the commanded current.

It is interesting to note that brushless motors have fewer armature coils than conventional DC motors. This is a function of implementation cost. Each armature phase requires 2 to 4 power transistors and the accompanying circuitry to drive them. It is therefore considered cost prohibitive to add armature coils in the quantity found on conventional motors. As a result, most brushless motors are built in two and three phase configurations.

2.3 Moog Brushless Motor and Torque Controller

The Moog motor used in this research is 3 phase wye connected. There are 8 Samarium Cobolt motor poles mounted on an internal rotor. Shaft position feedback is provided

by a brushless resolver attached to the end of the rotor shaft. The motor is capable of delivering 15 in.lb. continuous and 60 in.lb. peak torque. The motor constant is approximately $27 \text{ oz-in}/\sqrt{W}$.

The controller, shown in Figure 2.2 mounted in an equipment rack alongside its power supply, is configured for torque control. The 3 phases are sinusoidally driven by 320 volt 5kHz PWM current drivers. The current amplifiers can provide 15 amps continuous and 30 amps peak current. Peak output power is therefore approximately 10 kW. The resolver to digital converter provides 12 bit shaft position data and a velocity signal. While the motor is mechanically capable of spinning up to 11,000 rpm, the controller is configured for high resolution commutation and cannot drive it above 500 rpm.

The combined torque bandwidth of the controller/motor combination is approximately 90 Hz. The 90 Hz cutoff is a result of the motor inductance limiting response time. While the mechanical time constant of the motor is $\approx 1.0 \text{ mSec}$, the electrical time constant is $\approx 1.72 \text{ mSec}$.

The controller could be reconfigured to drive almost any 3 phase brushless motor subject to its power and voltage limitations. In order to do this, the commutation electronics would have to be modified to account for the motor pole count and the current loops would have to be tuned to be stable driving the new motor windings. A complete specification sheet and performance curve for the Moog equipment and a dimension sketch for the Moog motor is provided in Appendix I.



Figure 2.2 The Moog Torque Controller and Power Supply.

AD-A-209899

AD-A 809899 MISSING PAGES WILL BE INSERTED AT AN LATER DATE AS
ERRATA(S). PAGE(S) 23 & 24

10 MAY 1982

Minsky (1981) presented an argument for endpoint sensing in force control. He dismissed joint torque control due to perceived limitations in the ability to accurately identify and control inertial forces and the lack of resolution caused by noise in the joints. Minsky proposed that an endpoint sensor be combined with a "relaxed wrist" to control contact forces. As envisioned, a "relaxed wrist" would be a device with at least 3 degrees of freedom that could enable a manipulator to exhibit high compliance at its endpoint.

The concept of a "relaxed wrist" is remarkably similar to the work performed by Cannon et al (1986) on fast end effectors. The fast end effector was attached to the end of a flexible manipulator. Contact forces were controlled by an endpoint sensor and a force control loop closed around the fast end effector. In this way, the force control loop did not contain the dynamics of the whole manipulator allowing contact forces to be more readily controlled.

The research indicates that utilizing a wrist force sensor and closing a force loop around the manipulator dynamics, limits bandwidth and performance of contact force control. Force control loops should be closed more tightly around the fast end effectors of Cannon (1986), the "relaxed wrists" of Minsky (1981), or the individual manipulator joints. Closing torque loops at the manipulator joints appears to offer much promise in providing high bandwidth manipulator performance because 1) There are fewer enclosed manipulator dynamics to go unstable, 2) it is no longer necessary to insert a large compliance between the manipulator and the environment. 3) the inertial param-

eters can be identified with enough accuracy to allow good control of contact forces (An 1986), 4) the effects of large joint frictions and nonlinearities can be greatly reduced (Paul (1983)), and 5) finally, as An (1986) demonstrated, wrist force sensor feedback can still be utilized to increase accuracy in a joint torque control system without leading to dynamic instabilities. Therefore, it seems clear that one aspect of research in force control should concern itself with developing robust, repeatable, and accurate torque sources for use in force control implementations. The remainder of this thesis discusses issues involved with the accurate torque control of brushless motors.

3.2 Torque Measurement

One approach to torque control is to utilize a torque sensor and close a torque loop. This approach has been taken several times (Paul and Wu (1980), Luh, Fisher, and Paul (1983), Dalgetty (1984), and Lim (1985)). Paul's work involved designing and implementing joint torque sensors for the Stanford manipulator. The sensors were strain gauge based and were used primarily to close a torque loop around harmonic drives in order to reduce joint friction effects. Dalgetty and Lim both built torque sensors to be fitted to the MIT Direct Drive Arm (DDarm). Both designs were based on cantilever beams mounted to the motor shaft. Dalgetty's design consisted of an interesting dual sensitivity sensor. Unfortunately, the system was tough to calibrate and difficult to use. Dalgetty (1984) also investigated the coupling effects of sensor stiffness with manipulator dynamics and performance. Lim implemented a stiffer sensor which

exhibited good linearity and repeatability. He also developed a stable analog torque controller which reduced the standard deviation of the mean output torque to 0.1 % . Lim reported that the uncompensated Direct Drive Motor had ripples of ± 50 % of the mean output torque at the frequency of the motor pole pairs.

The first aspect of my research involved designing two torque sensors. The first sensor was a rotation limited fixture designed to measure motor output torque as a function of angle. The sensor served as a tool to study the nonlinearities in brushless motor torque and as a prototype to familiarize myself with issues in sensor design. The construction of the first sensor contributed a great deal to the successful design and assembly of the joint torque sensor that followed.

Shimano and Roth (1976) listed several attributes of a good sensor design. They indicated that a sensor should exhibit high stiffness, compact construction, good linearity, and low hysteresis and internal friction. For the first sensor, it was only necessary to match output torque, achieve good linearity and low hysteresis, and reasonable stiffness. Compactness of design was not really an issue.

Torque transducers are generally divided into two classes: 1) inline or 2) reaction type. While both classes involve measuring a torque induced displacement, inline sensors produce a signal based on the torque transmitted from the actuator thru the transducer to the load. Reaction type sensors, on the other hand, typically support the actuator or load and measure the transmitted torque as a function of the reaction forces.

The most common reaction type torque transducer is the torque deflecting table. Available commercially, the transducer supports the actuator and measures deflections in the supporting elements in order to infer output torque. Deflection measurement is typically achieved with strain gauges although Velayudhan (1984) describes a torque sensing table which utilizes a differential inductance transducer to measure displacement.

In this research, reaction type transducers were passed up in favor of inline designs. The reason for this was: 1) The use of reaction transducers necessitates inclusion of the motor housing mass in the sensor dynamics which adversely effects performance. 2) Development of a reaction type sensor might preclude integrating the motor housing into a manipulator structure. 3) An inline sensor could offer more flexibility in later sensor placement (i.e. the sensor could be placed on any shaft in a potential reducer mechanism).

The first sensor, shown on the motor shaft in Figure 3.1, was designed as an inline cantilever beam type sensor. In the sensor, semiconductor strain gauges are used to measure deflection, since they exhibit high sensitivity. The MicroGage strain gauges used in this research, have a gauge factor (change in resistance/strain) of 135Ω .

The sensor design involves attaching a cantilevered aluminum beam to the end of the motor shaft. A single strain gauge mounted on either side of the beam serves as each of two legs in a Wheatstone bridge. Motor torque exerts a bending moment on the beam which can be measured by the change in resistance in the strain gauges. An

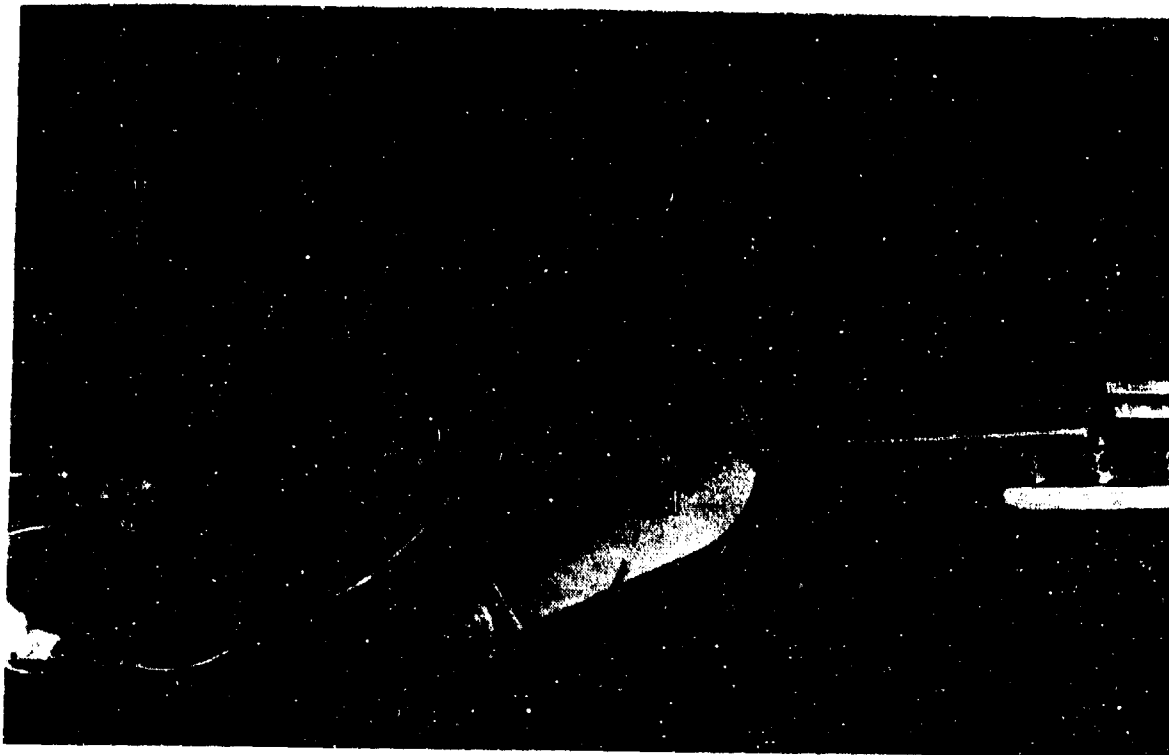


Figure 3.1 The experimental fixture used to measure output torques.

Analog Devices 521 Instrumentation Amplifier, accompanying trim pots, and precision resistors to serve as the remaining two legs of the Wheatstone bridge are carried on a circuit board attached to the cantilever beam. The location of the amplifier electronics is aimed at minimizing noise absorbed by the signal wires before the signal can be amplified. Shielding is only provided on the cable connecting the amplifier to the A/D converter. The bridge supply voltage is 5 volts.

Fixturing is included to allow output torque measurement as a function of motor shaft angle. The collar attached to the motor support bracket can be rotated through several turns in each direction. The cantilever beam is prevented from rotating freely

by two dowel pins protruding from the rotatable collar. The pins maintain a constant distance from the motor shaft and therefore allow the cantilever torque sensor to be calibrated.

The Wheatstone bridge sensitivity was designed to be $\approx 6\text{mV/in.lb.}$ The design allowed $1100 \mu\text{in/in}$ strain at the peak motor torque of 60 in.lb. The amplifier gain was set at 28 in order to provide a full scale output signal of ± 10 volts. A complete presentation of the cantilever sensor design equations is given in Appendix II.

Several lessons were learned from the design, construction, and operation of the first sensor. These lessons were used in planning the joint torque sensor. First, in order to double torque sensitivity, each leg of the Wheatstone bridge should consist of an active strain gauge. Second, each set of four gauges should be temperature coefficient matched so that the effect of thermal drift in the sensor gauge factors is canceled out by the bridge configuration. Third, the bridge itself and accompanying electronics should be shielded from EMI noise. Fourth, wire leads connecting the bridge to the amplifier should be as short as possible. Finally, the electronics should utilize fabricated copper trace boards and avoid wire wrapping in order to reduce noise and prevent short circuits. -

3.3 Development of a Joint Torque Sensor

The joint torque sensor was designed to provide good torque sensing characteristics, unlimited rotation, and compatibility with the cable driven manipulator design devel-

oped in our lab. The last criteria involved designing a sensor which could fulfill the functions of the motor output pulley of the cable driven manipulator. The pulley, shown in Figure 3.2, served several purposes in the manipulator design: 1) Provide a solid connection with the motor shaft (and prevent nonlinearities such as backlash). 2) Transmit power to the manipulator through the attached cables. 3) Allow attachment and tensioning of the manipulator cables through relative rotation of the pulley halves. 4) Provide the 3/4 inch outer diameter required to achieve the overall manipulator reduction ratio.

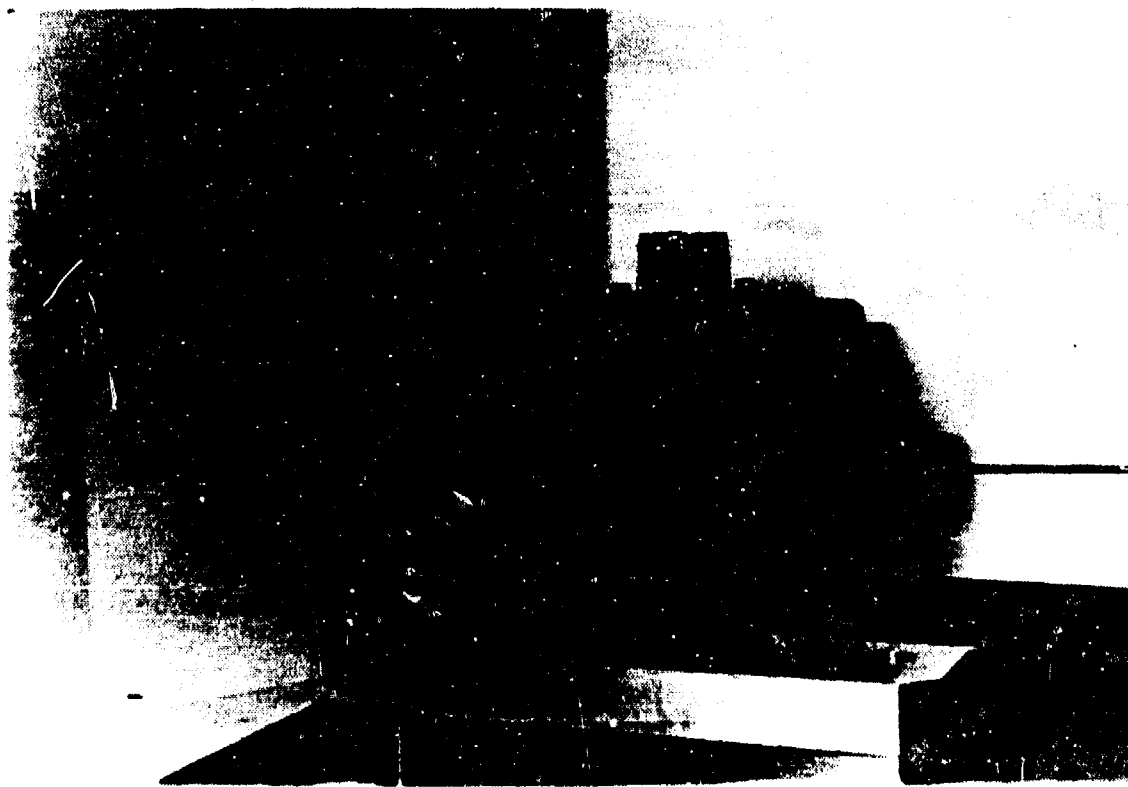


Figure 3.2 The output pulley on the cable driven manipulator.

In order to achieve a high level of performance, the design was approached from a systems standpoint. It was important to optimize the the mechanical sensing element,

the amplifying electronics, the electrical transmission system (including shielding), and the system as a whole, in order to achieve high quality torque sensing. A photograph of the completed sensor is shown in Figure 3.3. Figure 3.4 is a cutaway schematic of the sensor.

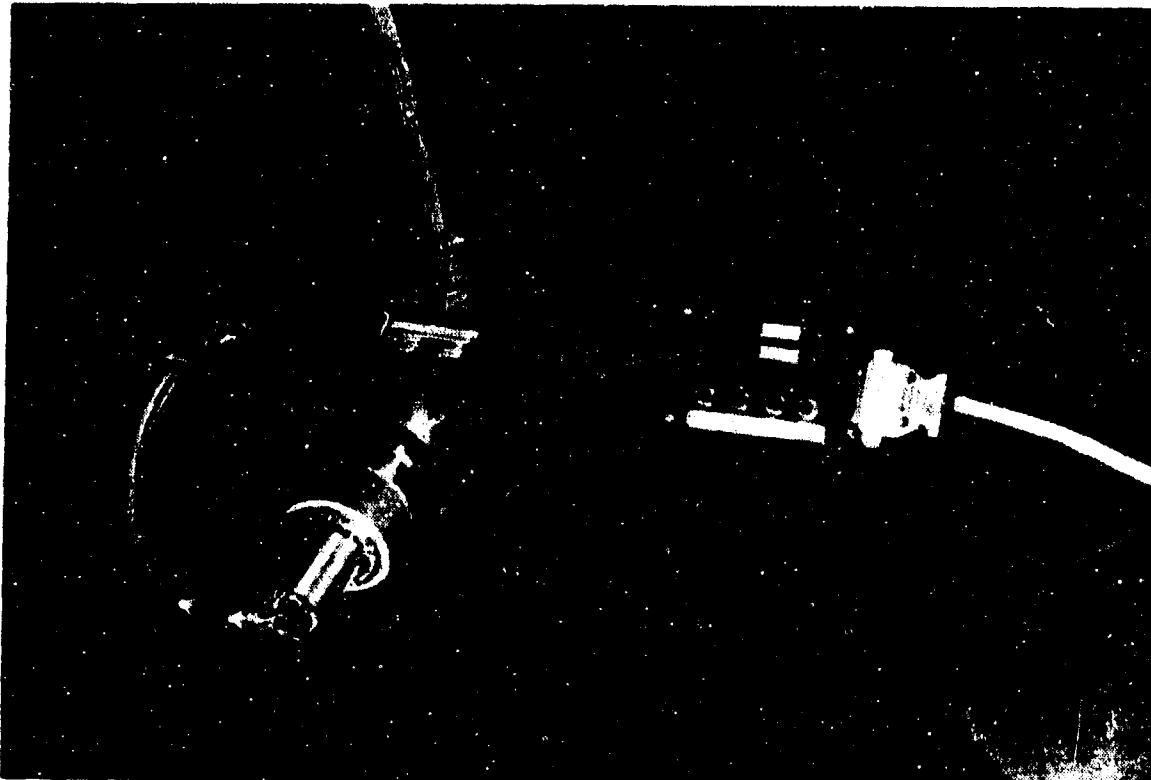


Figure 3.3 The joint torque sensor.

The mechanical sensing element was designed to provide a linear output proportional to motor torque as well as to reject the effects of transverse loading, bending moments, and axial thrust. Effort was also made to minimize overall rotational inertia of the sensing element. By limiting inertia, the acceleration performance of the cable driven manipulator would not be overly reduced by the addition of the sensor. In addition, it was important to avoid creating new low frequency vibration modes involving the

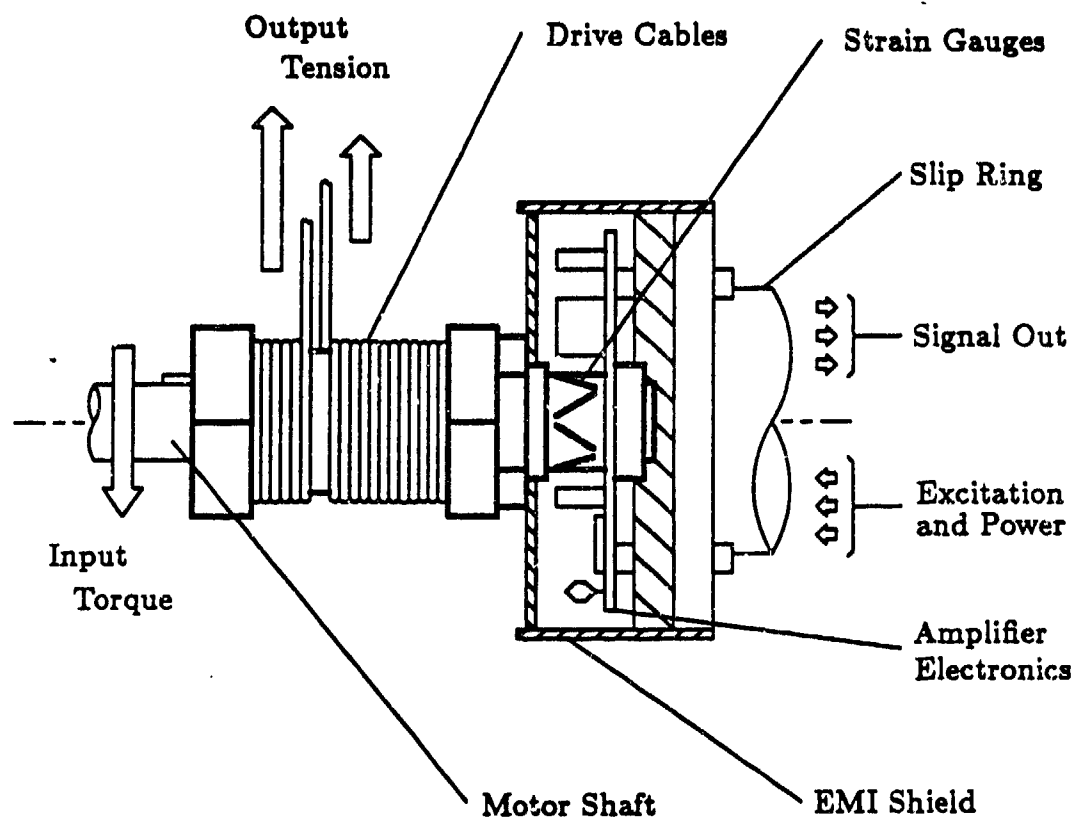


Figure 3.4 A schematic of the torque sensor showing cross sections of the main components.

sensor mass and its compliance or coupling with the manipulator dynamics (Dalgetty 1984) which would adversely affect manipulator control. The resulting design is shown in Figure 3.5.

There are six stainless steel parts in the mechanical sensing element. An exploded assembly is presented in Figure 3.6. The torque shaft couples to the motor shaft, provides the inner race for the caged needle bearing, and allows connection of the

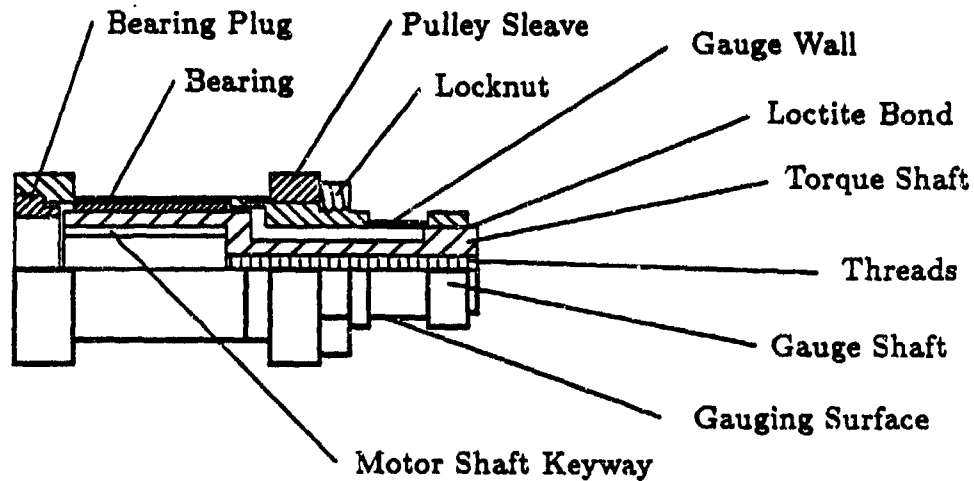


Figure 3.5 The mechanical sensing element.

amplifying electronics and slip ring. The gauge shaft is Loctited to the torque shaft at one end. It is the gauge shaft that contains the thinned hollow circular gauging, torque sensing section. Torque is transmitted down the torque shaft, across the Loctited joint, through the gaged gauge shaft section, and out through cables attached to the gauge shaft. The end of the gauge shaft with the cables is supported by a needle roller bearing in order to allow large transverse loads on the sensor. Like the torque shaft, the gauge shaft serves as a bearing raceway and is precision ground for accuracy.

The pulley sleeve can be rotated relative to the gauge shaft so that cable can be taken up and cable tension adjusted. Holes are machined in the pulley sleeve and gauge shaft where the cables are terminated and attached to the torque sensor. The locknut is tightened in order to secure the pulley sleeve to the gauge shaft and maintain cable

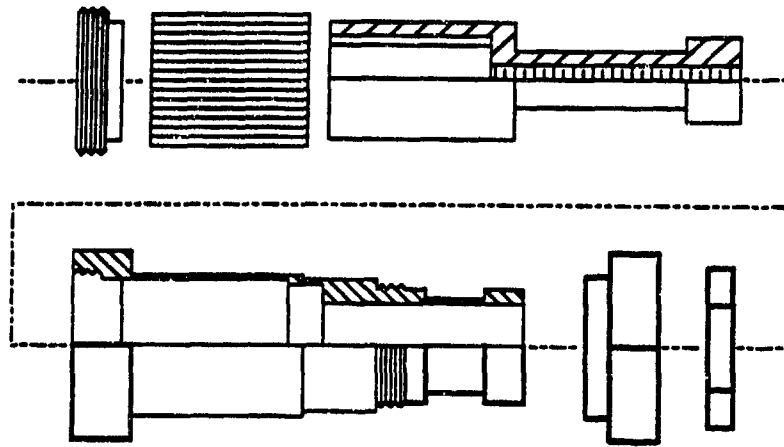


Figure 3.6 An exploded view of the mechanical sensing element.

tension. The locknut also provides an edge on which to seat the disk portion of the EMI shield enclosing the strain gauges and accompanying electronics. Finally, the hex head on the gauge shaft facilitates cable tensioning.

Two complete strain gauge based Wheatstone bridges are located on the gauge shaft. The gauges are cemented on the outer surface of the gauge section in the pattern illustrated in Figure 3.7. In each bridge, two strain gauges are mounted at 45° relative to the shaft axis and the other two are mounted at 135° . This orientation allows the gauges to measure the maximum tensile and compressive strains caused by applied shaft torque. At the same time, the orientation is not sensitive to strains caused by bending moments and axial loads.

The gauge portion of the gauge shaft is ≈ 0.006 in. thick. At a peak torque of 60 in.lb., each gauge is subjected to a strain of $1000 \mu\text{in}/\text{in}$. As with the static torque

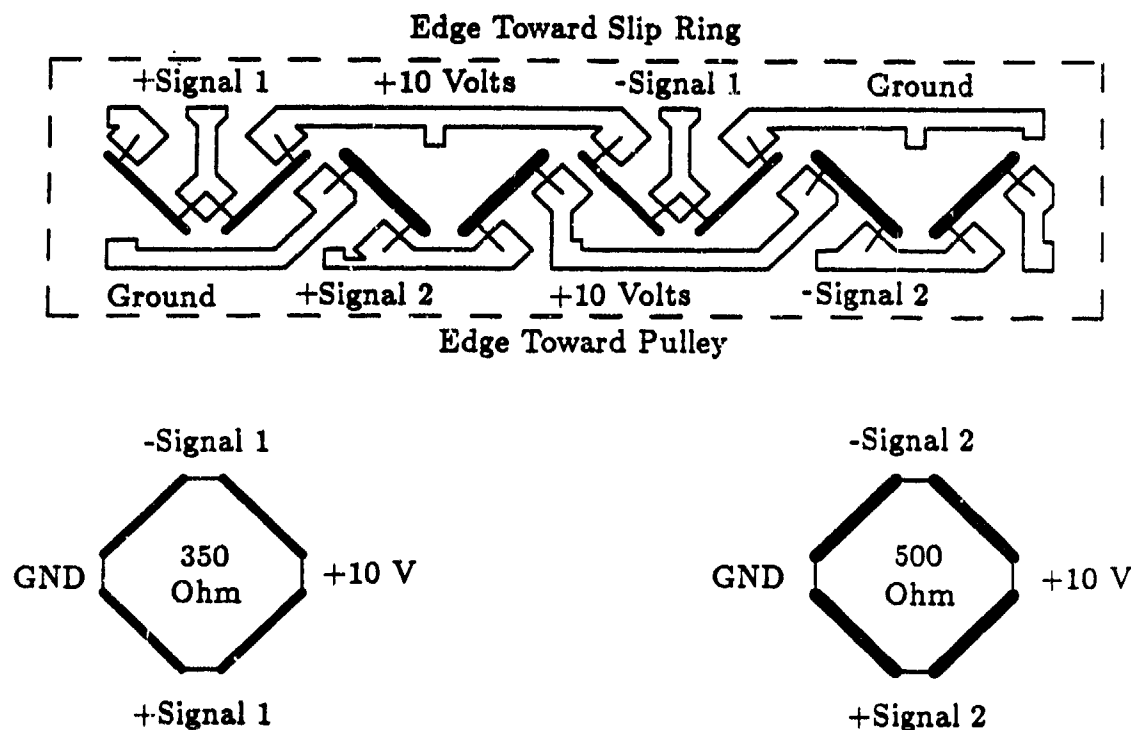


Figure 3.7 Strain gauge layout on the gauging surface.

sensor, this strain level is the maximum level recommended by Microgage for well defined peak loadings. While torque loadings on the manipulator are not well defined due to unanticipated impact and inertia loadings, it is felt that the compliance of the cables protects the sensor against overloads. The resulting torque sensor sensitivity is $\approx 10\text{mV/in.lb.}$ and is amplified to $\approx 170\text{ mV/in.lb.}$ by the instrumentation amplifier. The stress equations and design formulas for the joint torque mechanical sensing element are provided in Appendix III.

At the outset of the design, it was decided to utilize a slip ring to transmit power and signals to and from the rotating torque sensor. A rotary transformer was ruled

out in order to limit electronic complexity and required signal conditioning. Unfortunately, slip rings were known to produce white noise, mechanical friction, and vibration problems. White noise is undesirable because it degrades signal quality and it is not band pass filterable. This problem was addressed by amplifying each signal before the slip ring and by running each signal over four slip ring channels simultaneously and passing supply voltages through three channels. Redundant channels serve to reduce signal noise.

The friction problem was minimized by the slip ring manufacturer Michigan Scientific, which handpicked a slip ring from stock with a breakaway torque of less than one oz.in. Finally, the eccentricity induced vibration problem was reduced by designing an EMI shield which served to center the slip ring on the sensor axis.

The cylindrical EMI shield is positioned on the sensor by the protruding shoulder of the torque shaft. Bolted in place, the shield supports and locates the 20 channel slip ring. Three hollowed bolts run through the slip ring and the EMI shield to the amplifier circuit board. Power and signal lines are routed through the bolts to the sensor electronics. Another EMI shield covers the opening of the cylindrical shield. Both shields are constructed of an iron and copper laminate glued to the outside of ABS plastic support components. The laminate was donated by Chomerics, of Hudson, MA and is designed to attenuate both magnetic (iron) and electric (copper) field interference.

The sensor electronics, pictured in the photo of Figure 3.8, are mounted on an annular circuit board. Two surface mount AD 524 instrumentation amplifiers, which

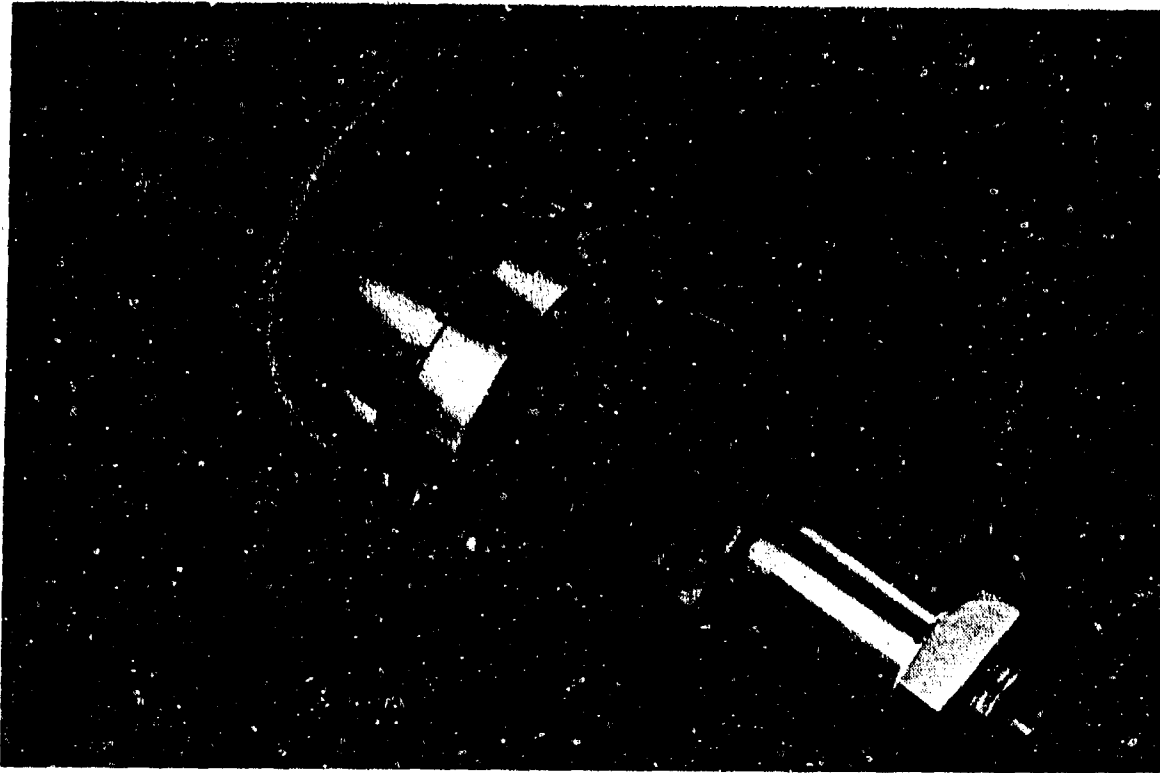


Figure 3.8 The joint sensor electronics.

have improved operating characteristics compared to the AD 521 IAs, amplify the output signal of each Wheatstone bridge. The board also carries input and output trim pots and bypass capacitors to filter the supply voltages. The annular board was commercially fabricated to insure its electrical and mechanical integrity during operation. It should be noted that the amplifiers were located on the rotating portion of the sensor for two reasons: 1) A design goal had been to amplify the bridge signals as soon as possible. 2) It was desired to increase the magnitude of the signal before the added noise of the slip ring channels.

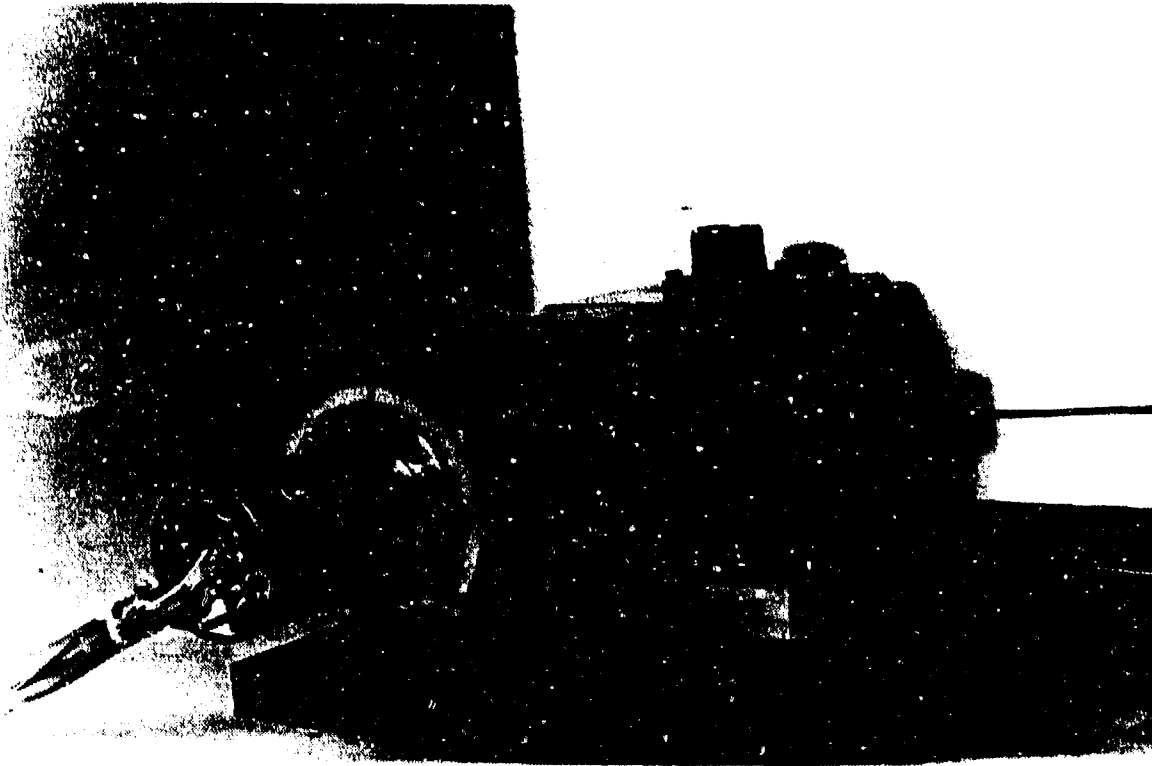


Figure 3.9 The completed torque sensor mounted on the Moog motor and integrated into the cable driven manipulator.

3.4 Signal Noise Reduction

Signal noise EMI generated by the 320 volt PWM controller was a large problem that had to be addressed. In certain areas in our lab, the 5 kHz PWM was capable of generating voltage spikes on the order of 50 volts in the surrounding signal lines. Theoretically, a 2-pole Butterworth active low pass filter could have removed the noise. Such a filter, with a cut off frequency of 50 Hz would reduce the noise 80 dB by design. Unfortunately, the PWM noise was everywhere. A filtered signal would have picked up unacceptable levels of noise between the filter and the A. D converter. In addition,

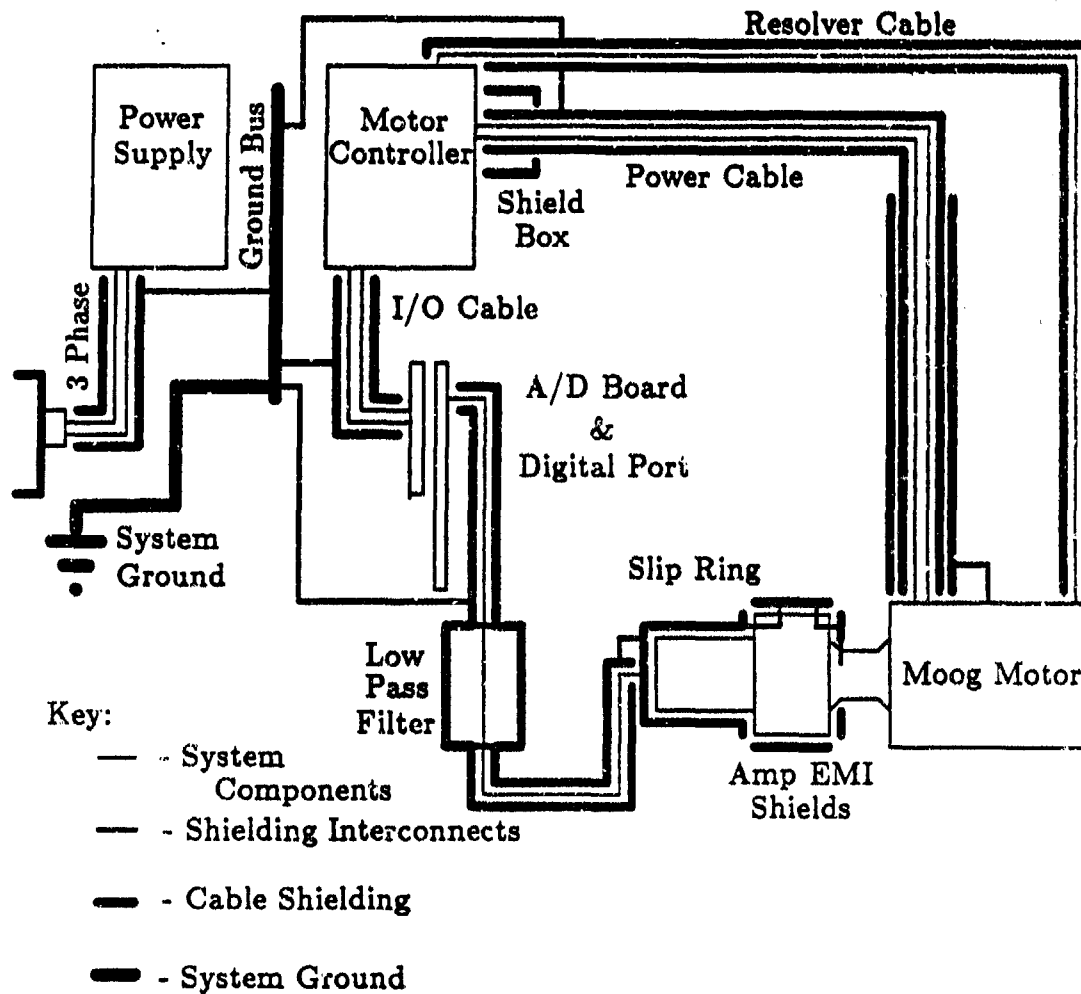


Figure 3.10 Schematic of the shielding system used in the lab.

it was desired to avoid low pass filtering on the torque sensor in order to avoid the resultant-phase lags and controller instability problems (Eppinger (1986)).

Another approach involved shielding both the EMI sources and the signal and voltage wires. Denny (1986) provides a good reference for shielding implementations. Figure 3.10 shows a schematic of the shielding system used to reduce EMI in the motor control system.

Four major steps provided excellent results in reducing noise: 1) A grounding bus bar was bolted to the equipment rack providing a low resistance grounding plane. 2) The bottom of the controller where the motor phase cables are connected was enclosed in a metal box. 3) The motor power cable was sheathed with braided copper cable, including a second layer at the outboard end. Initially, the cable had a single sheath and was grounded to the equipment rack, but in order to improve results and more completely attenuate the escaping noise near the torque sensor, a second layer was added and the shielding was grounded to the motor housing. While such a double ground is considered bad practice, it improved signal quality significantly. 4) The EMI shields on the motor, including both slip ring housings, were carefully grounded back through the slip ring, along the torque sensor cable shields, to the equipment rack. The mechanical torque sensor, and therefore the motor shaft, were also grounded through this route to maximize noise attenuation.

Chapter 4

Current Based Torque Control

4.1 Torque Inference from Phase Currents

Many researchers have utilized current sensing to infer motor torques. Paul (1973), developed a simple joint sensing technique which utilized a relationship between currents and joint torques. Asada (1983) noted that torque produced by the DDARM motors could be estimated from the phase currents. Asada (1984) went on to state that with a standard equation of the form:

$$\tau = K_t [I_a \cos(n\theta) + I_b \cos(n\theta + 120^\circ) + I_c \cos(n\theta - 120^\circ)] \quad (4.1)$$

where $I_a, I_b,$ and I_c are the phase currents, K_t is the torque constant, n is the number of motor pole pairs, and θ is the mechanical angle of the motor shaft, one could achieve torque control within $\pm 10\%$ on the DDARM. He noted that the unmodeled error arose from: a) variation in the magnetic field in the air gap, b) distortions of the sinusoidal phase currents, and c) variations in the current sensing resistors. Finally, he reported (1984) that if the above equation was modified to account for rotor and stator slots, torque error could be reduced to $\pm 6\%$ of the mean torque. Unfortunately, he

did not outline the method used to compensate for rotor and stator slots.

Lim (1985) noted that while torques on the DDARM could be estimated using current sensing techniques, significant torque ripple and deadband nonlinearities degraded control performance. He noted that the nonlinearities were generally difficult to accurately identify and recommended that a torque sensor was necessary for precision torque control of the DDARM.

An (1986) ignored the nonlinearities of current based torque sensing and utilized the technique in his thesis research. Torques inferred from phase current sensing were used for inertial parameter estimation and feedforward torque control implementation. An (1986) reported that his force control scheme, utilizing joint torque control and wrist force sensor feedback, exhibited limits in accuracy attributable to torque ripple, deadband, and cogging torque.

4.2 Sources of Torque Ripple

Many fingers are pointed when the sources of torque ripple in brushless motors are described. Some point to stator slots causing variations in air gap reluctance which lead to cogging torque. Others point to saturation of iron laminations in the magnetic circuit or degradation of the magnetic flux due to the temperature dependence of the magnets. Others point to controller nonlinearities, and finally, others attribute torque ripple to nonsymmetric demagnetization of rotor magnets due to armature reaction (Aha (1987), Perret, Le-Huy, and Feuillet (1986), and Asada and Touni (1987)). Undoubtedly, all

of these factors play some role in the production of torque ripple. It is also pretty clear that different factors assume different degrees of importance depending on the individual application. It is my contention that in the interests of accurate torque control, the major factors should be accurately identified and compensation techniques should be developed when possible.

My research has shown that it is possible to utilize compensation techniques and phase current waveform modification to provide accurate torque control based on phase current sensing. Experimental results have indicated that accurate motor torque control can be accomplished through precise current sensing and control. In my lab work with a Moog brushless motor and controller the most significant causes of torque ripple have been identified. With this knowledge, it has been demonstrated that a significant portion of the torque ripple can be removed. While some of the corrections have a transient benefit and lose their effect over time, their initial effectiveness indicate that with controller modifications, the technology is now available to accurately control brushless motor torque through current control.

Figure 4.1 shows experimental data of the torque ripple on an uncompensated Moog 303-003 motor as a function of shaft angle. In the following paragraphs, I will attempt to outline the major factors contributing to this ripple. Accompanying the description of each factor, is a similar figure showing an experimental measurement of the associated ripple. The ripple magnitude is noted as a percentage of mean output torque.

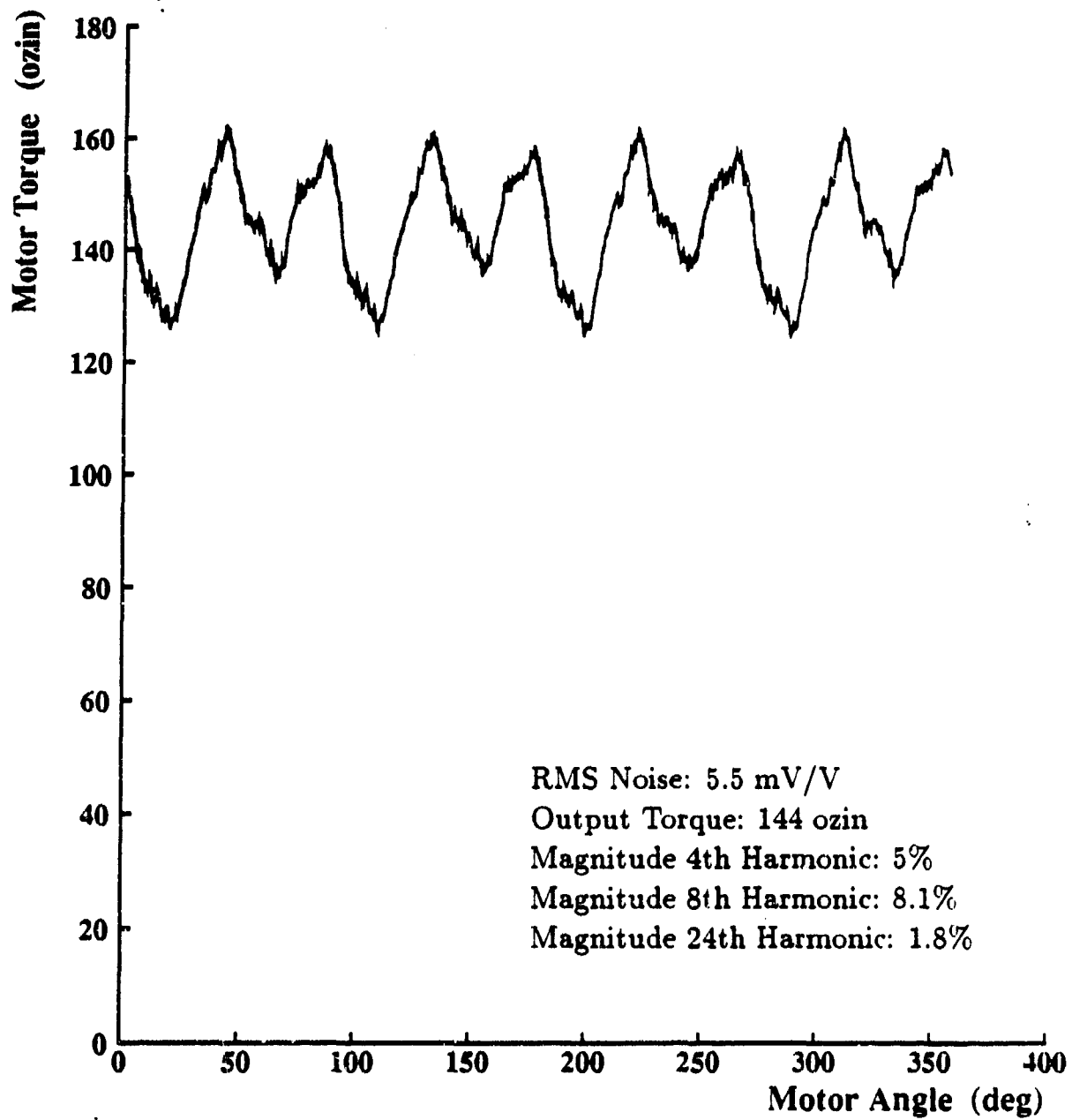


Figure 4.1 Torque ripple characteristics of the Moog controller and motor combination without compensation.

Torque ripple components in the output of the Moog 303-003, can be divided

into two categories: 1) ripple attributable to effects originating in the motor controller and 2) ripple resulting from the motor configuration and construction. In order to understand these effects, we must investigate the equation most commonly used to describe the torque output of a 3-phase brushless motor as a function of phase current. However, in the interest of clarity, we will present the equation in a slightly different form:

$$\tau = K_t [I_a \ I_b \ I_c] [S_a \ S_b \ S_c]^T \quad (4.2)$$

where τ is the output torque, K_t is the torque constant, $I_a, I_b,$ and I_c are the phase currents, and $S_a, S_b,$ and S_c are the spacial harmonics of the motor corresponding to each phase. Typically, the spacial harmonics are defined as:

$$\begin{aligned} S_a &= \cos(n\theta) \\ S_b &= \cos(n\theta + 120^\circ) \\ S_c &= \cos(n\theta - 120^\circ) \end{aligned} \quad (4.3)$$

where n is the number of motor pole pairs and θ is the mechanical angle of the motor shaft. Given the 3-phase wye connection of the motor, I_c is constrained according to Kirchoff's current law as:

$$I_c = -(I_a + I_b) \quad (4.4)$$

Most motors are driven with a first order approximation of the phase current waveforms needed for linear torque production. The first order approximation is:

$$\begin{aligned} I_a &= I \cos(n\theta) \\ I_b &= I \cos(n\theta - 120^\circ) \end{aligned} \quad (4.5)$$

Given the above assumptions, the computed theoretical torque is,

$$\tau = \frac{3}{2} K_t I \quad (4.6)$$

and independent of θ . A more meaningful derivation of the torque equation results if one defines the phase currents in the following way:

$$I_a = A \cos(n\theta) + \delta_a \quad (4.7)$$

$$I_b = B \cos(n\theta + 120^\circ) + \delta_b$$

allowing offset errors and relative waveform magnitudes to be included in the derivation of τ . The physical constraints of the motor windings insure that Equation 4.4 applies regardless of the individual current waveforms. Therefore, by defining the currents in phase a and phase b we have uniquely defined the current waveform in phase c. Given Equations 4.2, 4.4, and 4.7, the output torque becomes,

$$\begin{aligned} \tau &= \frac{3K_t}{2} (A \cos^2 \theta + B \sin^2 \theta) \\ &+ \frac{\sqrt{3}}{4} (B - A) \sin(2\theta) \\ &+ \sqrt{3} (\delta_a \sin(\theta - 120^\circ) - \delta_b \sin(\theta)) \end{aligned} \quad (4.8)$$

If the two phase current waveform magnitudes, A and B, are equal to a given value I and δ_a and δ_b are zero, then the output torque reduces to the value given in Equation 4.6. On the other hand, if the waveform magnitudes are unequal, $A = B + \Delta_a$, and $\delta_a = \delta_b = 0$ then:

$$\tau = \frac{3}{2} K_t B + \frac{3}{2} K_t \Delta_a \cos^2 \theta - \frac{\sqrt{3}}{4} K_t \Delta_a \sin(2\theta) \quad (4.9)$$

But since $\cos^2 \theta = \frac{1}{2} + \frac{1}{2} \cos 2\theta$, Equation 4.9 can be rewritten as:

$$\tau = \frac{3}{2} K_t (B + \frac{\Delta_a}{2}) + \frac{\sqrt{3}}{2} K_t \Delta_a \cos(2\theta - 30^\circ) \quad (4.10)$$

Equation 4.10 demonstrates that a difference in the current waveform magnitude of two phases in the motor, generates a torque ripple at twice the fundamental driving frequency of $n\theta$. For comparison purposes, a 5% variation in the phase current magnitudes will cause an $\approx \pm 3\%$ ripple torque at a frequency of $2n\theta$. In the Moog 303-003, such a ripple would cycle at 8θ and have a magnitude of $\approx \pm 7\text{oz.in.}$ at continuous output torque. Figure 4.2 shows the 8θ component of the ripple torque for the Moog motor.

The $2n\theta$ ripple derived above is an example of the more general case. By superimposing an $n\theta_\delta$ sinewave on a primary and feeding phase, one can produce a $2n\theta$ output torque ripple at any 30° increment phase angle. A primary phase is defined here as that phase whose fundamental waveform magnitude is increased by the addition of the $n\theta_\delta$ sinewave and the feeding phase is defined as that phase which provides the pathway for the $n\theta_\delta$ sinewave current to flow to the primary phase.

The imposed ripple magnitude is controlled by the amplitude of the superimposed $n\theta_\delta$ sinewave. The phase of the ripple is a function of the primary phase (i.e. phase A in the derived example) and the feeding phase (i.e. phase c in the derived example). In the derived example, the feeding phase was chosen by default, since phase B was not altered and wye construction requires that the $n\theta_\delta$ feeding current be drawn through phase C. The phase of the produced ripple can be controlled to a greater resolution by apportioning the $n\theta_\delta$ feeding current between both nonprimary phases and therefore rotating the $2n\theta$ torque vector between the 30° increments.

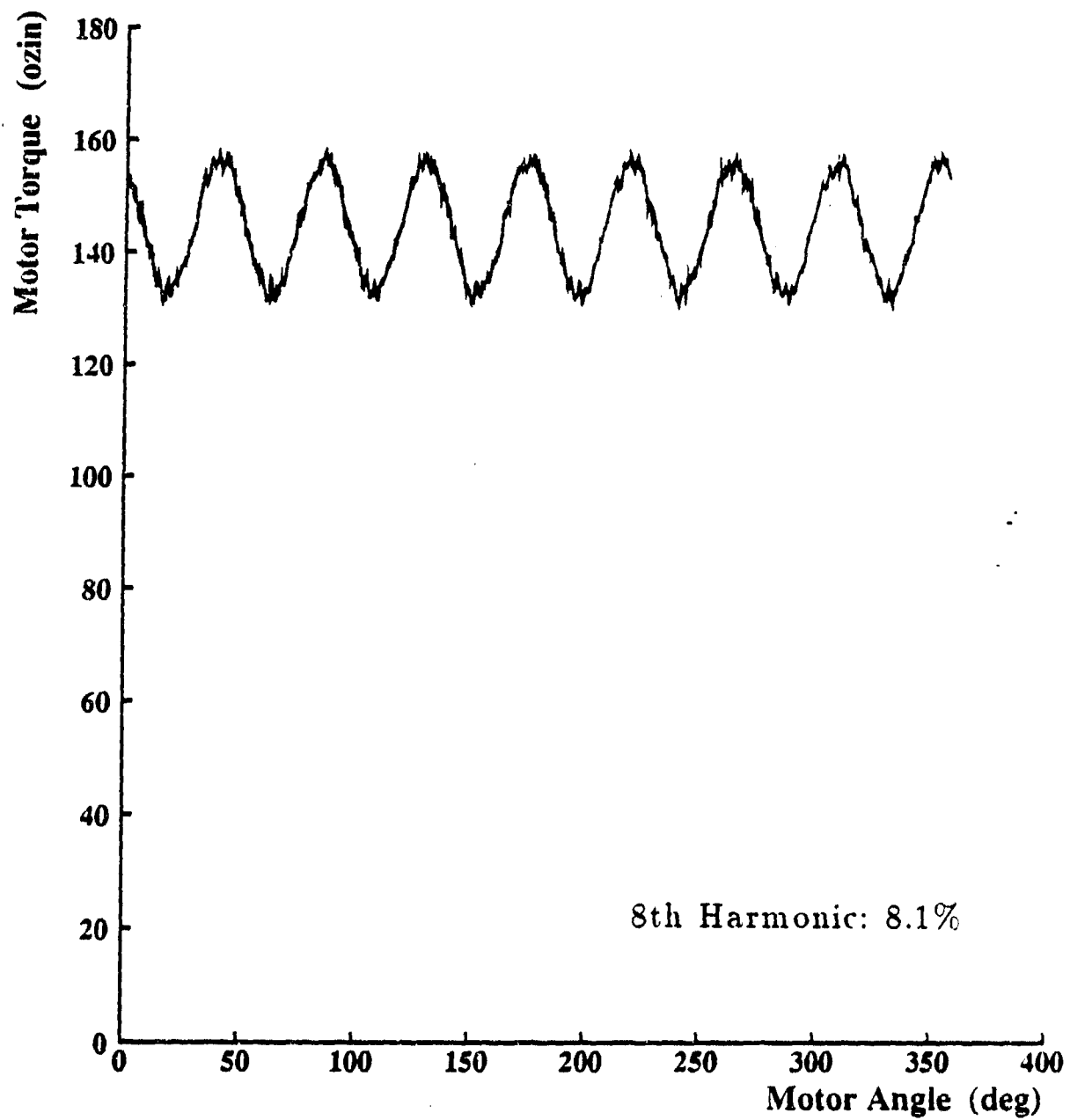


Figure 4.2 The $2n\theta$ Moog motor ripple component.

Another source of torque ripple arises when the fundamental current waveform of one or more phases is offset from zero. This situation is modeled by setting A and B

equal to I, but letting $\delta_a \neq 0$. We obtain the following result:

$$\tau = \frac{3}{2} K_t I + \frac{\sqrt{3}}{4} \delta_a K_t \sin(\theta + 120^\circ) \quad (4.11)$$

Clearly, the waveform offset produces a ripple at the fundamental frequency $n\theta$. The relative magnitude for a 5% offset would be $\approx \pm 6\%$. One should note that in a motor with offsets in all three phases, the effect is to alter the phase and magnitude of the $n\theta$ ripple without affecting its frequency. Figure 4.3 shows the 4θ component ripple for the Moog motor.

Current loop deadband is another controller nonlinearity that should be considered significant. Theoretically, it is difficult to model current loop deadband accurately. Therefore, an experimental approach was taken in which deadband was simulated in the controller's commutation tables and the resulting motor output torque was analyzed. The results indicate that current loop deadband produces torque ripple at all the integer multiples of the fundamental phase driving frequency $n\theta$. Figure 4.4 shows torque measurement results for the Moog motor with simulated (via table alteration) deadband in the current drivers.

Some of the torque ripple can also be attributed to motor construction. My research indicates that the most significant torque ripple arising from motor construction is caused by unmodeled spacial harmonics arising from imperfections of the physical implementation of the fundamental spacial harmonic. The unmodeled harmonics are actually odd harmonics of those modeled in Equation 4.1. The fact that the harmonics are odd results from the symmetry of the underlying motor construction. Equation 4.3

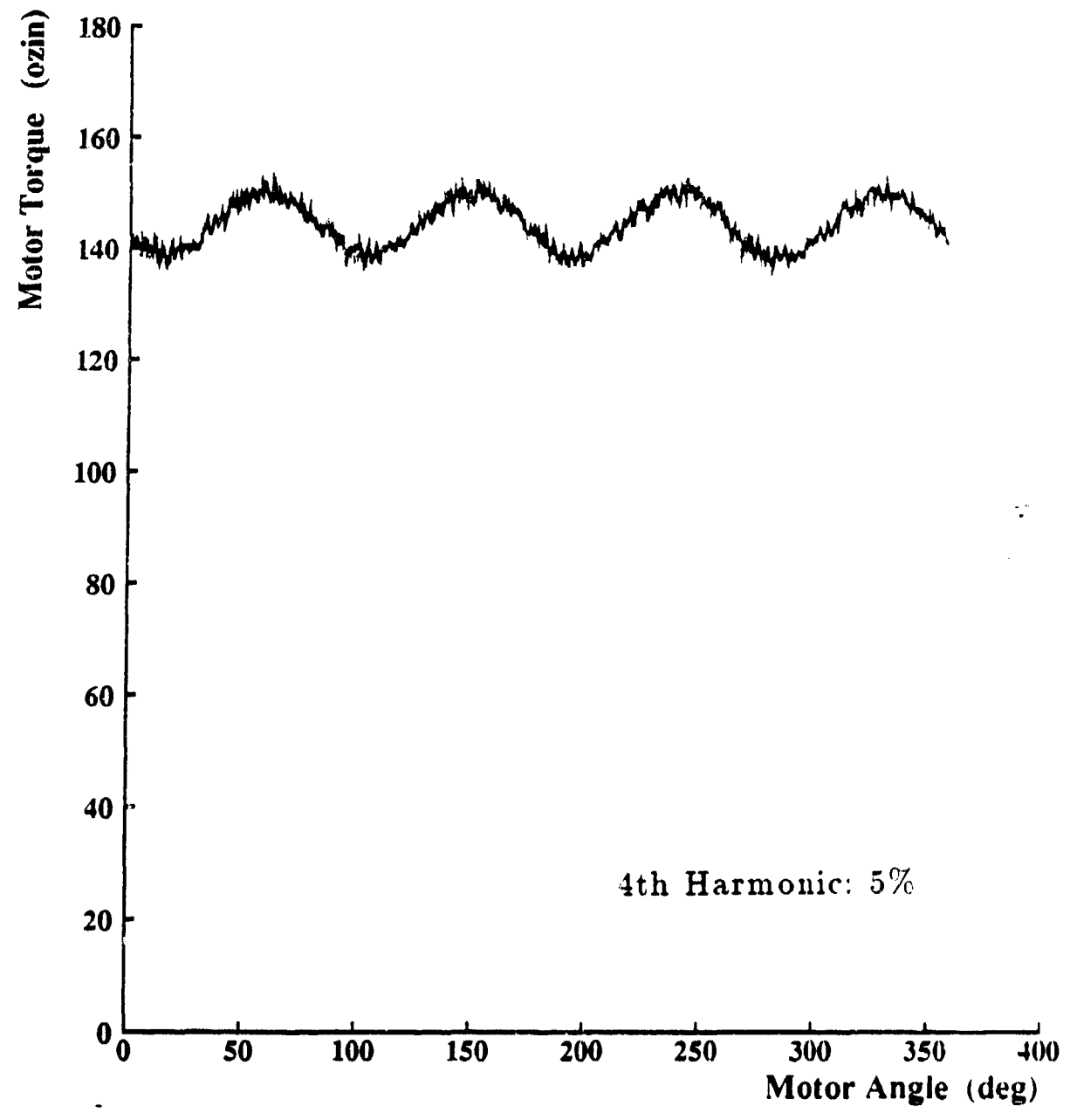


Figure 4.3 The $n\theta$ Moog motor ripple component.

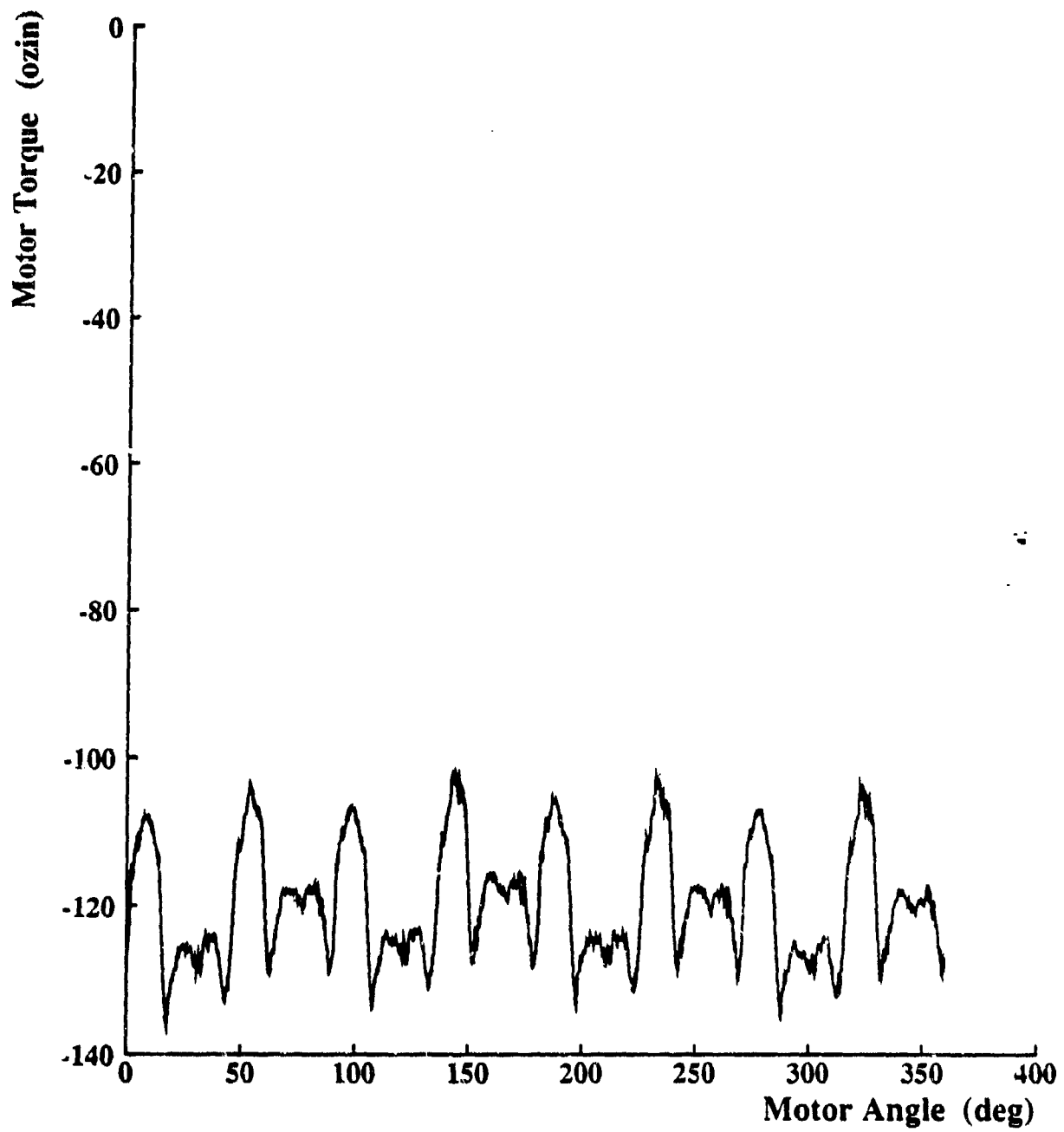


Figure 4.4 Torque ripple resulting from deadband in the current drivers. Note that this data is not a component of Figure 4.1.

should be represented as:

$$\begin{aligned}
 S_a &= S_1 \cos(n\theta) + S_3 \cos(3n\theta) + S_5 \cos(5n\theta) + \dots \\
 S_b &= S_1 \cos(n\theta + 120^\circ) + S_3 \cos(3n\theta) + S_5 \cos(5n\theta - 120^\circ) + \dots \\
 S_c &= S_1 \cos(n\theta - 120^\circ) + S_3 \cos(3n\theta) + S_5 \cos(5n\theta + 120^\circ) + \dots
 \end{aligned} \tag{4.12}$$

where S_1 is 1.0 and S_3, S_5, \dots are given as normalized values in relation to S_1 . These odd harmonics induce torque ripple in the motor, unless compensating higher order waveforms are superimposed on the fundamental commutation waveform. Equation 4.13 and 4.14 indicate how the odd harmonics produce torque ripple in an uncompensated system. Equation 4.13 presents the output torque with the spacial harmonics modeled and unmodified fundamental waveforms:

$$\begin{aligned}
 \tau &= \frac{3}{2} K_t I [S_1 - S_5 \cos(6n\theta) - S_7 \cos(6n\theta) \\
 &\quad + S_{11} \cos(12n\theta) - S_{13} \cos(12n\theta)]
 \end{aligned} \tag{4.13}$$

Note that the spacial harmonic harmonics of order 3 and multiples thereof do not induce ripple due to the three phase construction. Now, if harmonics are added to the commutation waveforms:

$$\begin{aligned}
 \tau &= \frac{3}{2} K_t [I_1 S_1 + I_5 S_5 + I_7 S_7 + I_{11} S_{11} + \dots] \\
 &\quad + \frac{3}{2} K_t [I_1 S_5 - I_1 S_7 + I_5 S_1 - I_7 S_1 + \dots] \cos(6n\theta) \\
 &\quad + \frac{3}{2} K_t [I_1 S_{11} - I_1 S_{13} + I_5 S_7 - I_5 S_{17} + \dots] \cos(12n\theta) \\
 &\quad + \dots
 \end{aligned} \tag{4.14}$$

Note that the lowest order ripple torque produced by the unmodeled harmonics is $6n\theta$.

This component of the ripple torque for the Moog motor is shown in Figure 4.5.

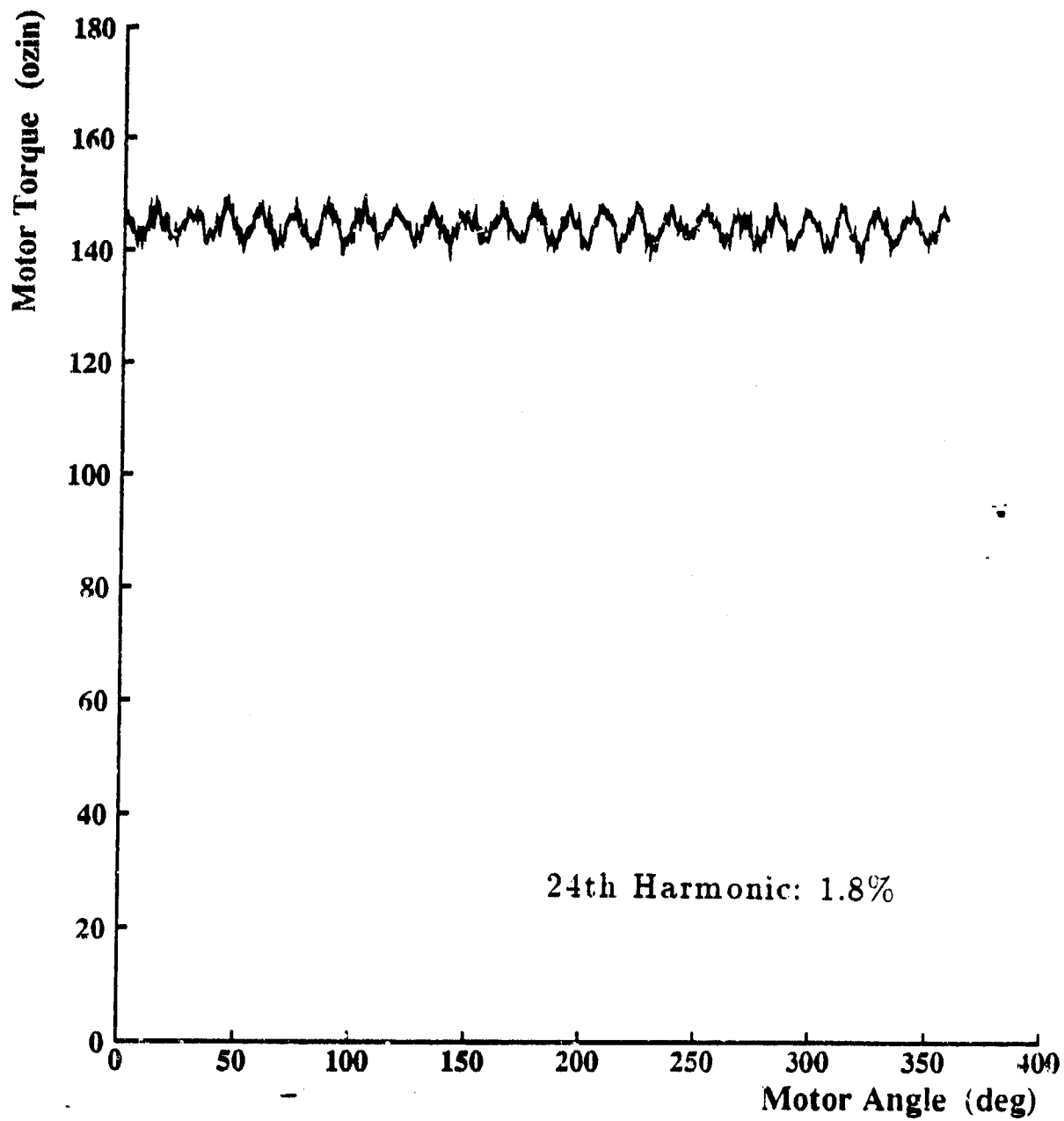


Figure 4.5 The $6n\theta$ Moog ripple harmonic.

If one assumes that only the fifth and seventh harmonic of the fundamental spacial

harmonic are significant, one arises at Equation 4.15 to describe the output torque.

$$\begin{aligned} \tau = & \frac{3}{2} K_t [I_1 S_1 - I_5 S_5 + I_7 S_7] \\ & + \frac{3}{2} K_t [I_1 (S_5 - S_7) + S_1 (I_5 - I_7)] \cos(6n\theta) \\ & + \frac{3}{2} K_t [I_1 S_7 + I_7 S_5] \cos(12n\theta) \end{aligned} \quad (4.15)$$

The odd harmonics can be identified by measuring motor torque as a function of easily controlled constant phase current vectors. For example, one of the phases can be physically disconnected (this protects against undetected current flows) while a constant current value is maintained through the other two. The resulting torque is practically a finger print of the complete spacial harmonics of the motor. By performing a Fast Fourier Transform (FFT) on the output torque as a function of motor angle, one obtains a listing of the relative magnitudes of all spacial harmonics within the sensitivity limitations of the torque sensor.

Le-Huy, Perret, and Feuillet (1986) provided a very good description of harmonic induced torque ripple. They suggested a method to minimize the ripple by modifying the commutation waveforms. In their work, they identified the significant spacial harmonics of a 3-phase disk-type brushless motor with trapezoidal flux distribution. Their approach involved monitoring the phase winding back EMF in order to model the spacial harmonics. They applied their technique to their motor and reported a 70% reduction in the lowest frequency harmonic induced ripple component.

4.3 Torque Ripple Compensation

There are many approaches that can be taken for torque ripple compensation. The first approach taken in my research was to characterize the output torque and scale torque commands given to the Moog motor controller based on motor rotor position. In order to accomplish this, a lookup table was assembled which contained the effective motor torque constant at various motor shaft angles.

It was desired to more accurately identify the causes of torque ripple and reduce their effects by altering the commutation waveforms. By accomplishing this, the Moog motor controller would become a black box that would produce a torque proportional to the input command. Moreover, the modified commutation waveforms would improve torque production performance and attenuate most of the nonlinear effects in the torque output.

The simplest path to such a goal involved closing a torque control loop around the motor and controller, driving the torque controlled controller/motor combination to achieve a constant output torque, and then recording the phase current waveforms for later use in phase commutation. This technique, suggested as a first pass type solution by a good friend Leo Casey, is very pragmatic and quite effective (as outlined in Chapter 5). On the other hand, from a theoretical standpoint, the approach is not very clean. The problem lies in the fact that the uncompensated controller and its inherent nonlinearities, are driven to eliminate those same nonlinearities. The end result is that

the form of the derived commutation waveforms is not clearly linked to the resulting improvement in torque control linearity. The clearest example of this is the fact that phase commutation waveforms produced by this technique, are slightly offset in phase angle and no longer correspond in phase to the motor spacial harmonics. Such an effect unnecessarily lowers overall efficiency and obscures the fact that the nonlinearities are not caused by misorientation of commutation phase angles. Overlooking such arguments, it should be pointed out that from a practical standpoint, this technique provides very good output torque linearity. In addition, it is probably the best practical technique for compensating for current loop deadband.

The final technique adopted in this research, involved modifying the commutation waveform lookup tables used by the Moog controller, in order to remove sources of torque ripple. This involved: 1) Adding in offsets to remove phase leakage resulting from nonzero δ_a and δ_b values as presented in Equation 4.7. This attenuated the 40 frequency ripple found in the Moog motor. Eventually, this aspect of the compensation was implemented in hardware. 2) Adjusting the relative magnitudes of the commutation waveforms in order to account for the Δ_a value used in Equations 4.9 and 4.10. 3) Finally, superimposing higher order harmonics on the fundamental commutation waveform, in order to compensate for harmonic induced torque ripple.

As noted by Le-Huy et. al. (1986), given a 3-phase wye connected brushless motor with no neutral connection, current harmonics at integer multiples of three of the fundamental frequency cannot be produced. Therefore, harmonic compensation is

accomplished with the 5th, 7th, 11th, etc. harmonics of the fundamental frequency. Le-huy (1986) and his colleagues provided a solution technique for choosing the optimal magnitude of these compensating harmonics based on the back EMF frequency components. One of their concerns was to limit the magnitude of any one harmonic to 10% of the fundamental. This is only an issue with motors designed with a trapezoidal flux distribution. The Moog motor, was designed for sinusoidal flux distribution and therefore the spacial harmonic harmonics are too small to require magnitude limits on their compensating current forms.

The approach taken to harmonic compensation in my research was similar in principle to the approach taken by Le-Huy et. al. The odd harmonics were identified through torque measurements and their magnitudes were normalized in terms of the fundamental spacial harmonic. Current waveforms of the same normalized magnitude (in relation to the fundamental current waveform) were then superimposed on the commutation waveform. Current harmonics were added only to correspond to those spacial harmonics considered significant in terms of the production of ripple torque.

Chapter 5

Results

5.1 Torque Sensor Results

The cantilever sensor was extremely useful in my research. After calibrating the sensor with weights, the amplifier gain was adjusted to make a 60 in.lb. applied torque appear as a 10 volt torque signal. The sensor proved to be both stable and linear. In addition, the rotating collar allowed motor torque data to be easily recorded at various shaft angles. Most of the torque data for this thesis research was obtained with the cantilever sensor.

Several problems were encountered. First, the basic design of the sensor did not properly address the issue of noise isolation. As a result, in order to generate useful data, it was necessary to pass the generated torque signal through a 3 stage low pass RC filter network. Later, a 6 pole active Butterworth filter, with a cut off frequency of 50 Hz was built to remove noise more effectively. In addition, it became clear that shielding the signal, voltage supply lines, and motor power cable would be necessary to optimize joint torque sensor performance. Another problem concerned mechanical

backlash in two areas: 1) The shaft keyway allowed a slight rotation between the cantilever sensing element and the motor shaft and 2) The dowel pins on the rotating collar did not fully constrain the cantilever tip. The backlash produced aberrant results when the cantilever sensor was used to identify the motor harmonics. Therefore, this portion of the research was performed with the joint torque sensor.

Other aspects of the cantilever design, while not creating significant problems, presented opportunities to improve the joint torque sensor design. First, it was clear that full Wheatstone bridges would double torque sensitivity and eliminate the need to provide matched resistors for the third and fourth bridge leg. Moreover, the use of full bridges would eliminate some lead wire and reduce the associated EMI noise. In addition, by choosing temperature coefficient matched strain gauges, the effects of thermal drift would be canceled by the bridge configuration and not affect the sensor output.

The second opportunity for improvement lay in having the sensor electronics board fabricated. In the cantilever sensor, the electronics were wire wrapped and probably held up much longer than I deserved. I decided that a fabricated board would be much more reliable and should be produced for the joint torque sensor.

The joint torque sensor was assembled with one design modification. It was initially intended that the slip ring would be attached to the plastic EMI shield bolted on the sensor torque shaft. Unfortunately, the manufactured shield did not provide the necessary positional accuracy and the slip ring was prone to excessive runout and axis

misalignment during operation. In order to remedy this, the EMI shield was converted to a simple tube shape and a precise aluminum disk was machined to attach the slip ring to the sensing element. The modification reduced runout to 0.002 in. and virtually eliminated shaft misalignment.

Upon assembly, one of the strain gauge bridges proved to be all but useless. The 500 ohm bridge exhibited large thermal drift and was therefore disconnected. The 350 ohm bridge on the other hand, was very resistant to drift problems. This is probably a result of the efforts at Micro Gage to match the thermal coefficients of each sensor in a four gauge set.

The linearity of the resulting joint torque sensor is illustrated in the calibration curve of Figure 5.1. RMS error was ≈ 0.034 volts or ≈ 3 oz.in. Calibration was accomplished with a somewhat crude spring force gauge and pulley system.

The signal noise level in the joint torque sensor signal was greatly improved when compared to the cantilever beam sensor. Unfiltered RMS noise levels were approximately 10 mV for the joint torque sensor as compared to unfiltered RMS levels of ≈ 0.5 V on the cantilever sensor. Such low noise levels allowed the joint torque sensor to be used in an unfiltered mode although oftentimes data was recorded with the Butterworth filter lowpassing the signal. High signal quality and minimal backlash effects allowed the sensor to be utilized effectively in identifying the motor spacial harmonics. In addition, motor torque could be controlled within $\approx 1\%$ by digitally closing a torque control loop around the motor and torque sensor.

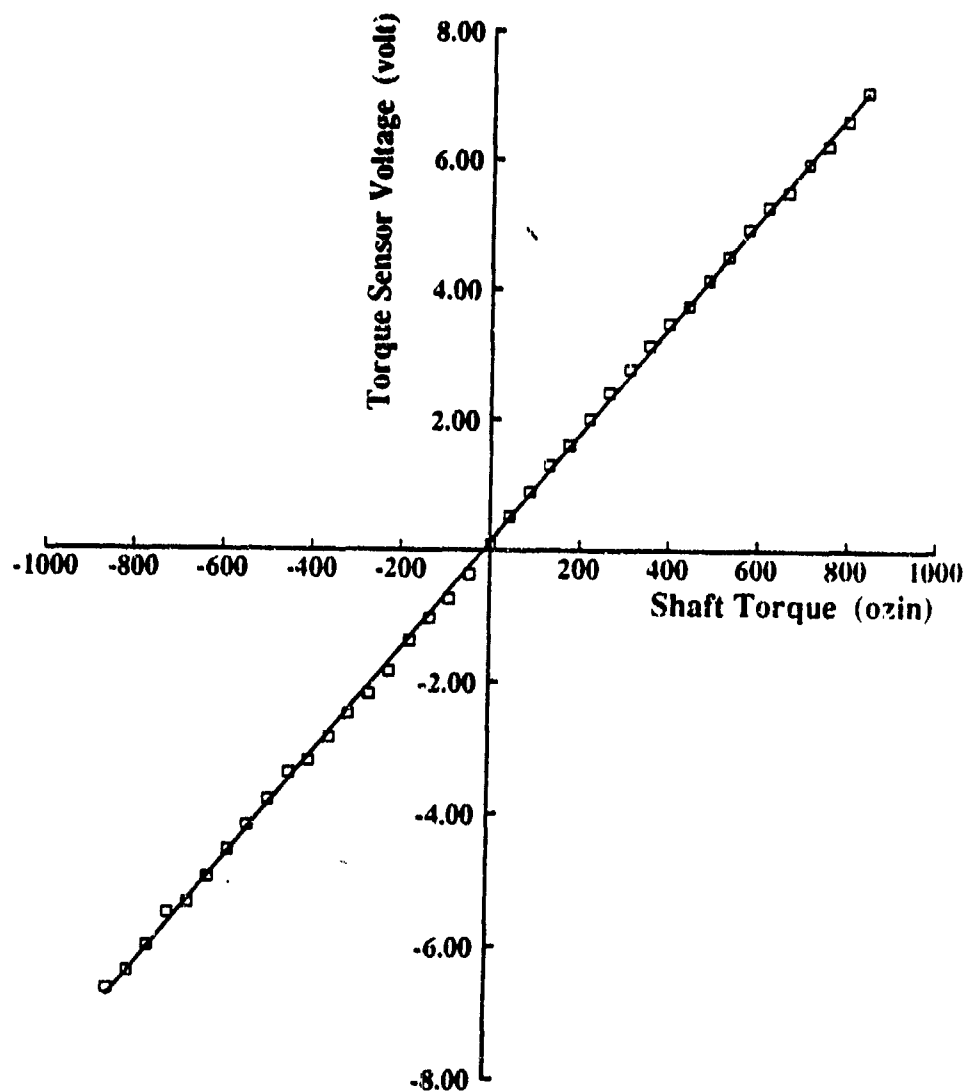


Figure 5.1 Joint torque sensor calibration curve.

The keyway problem was greatly improved through more accurate machining. Unfortunately, unless the shaft was bonded to the sensor, keyway backlash effects were still noticeable. Figures 5.2-5.6 show sinusoidal torque controller commands at 1, 5, 10, 25, and 50 Hz and the resulting torque sensor output with the output pulley locked in one position. Two characteristics are noticeable. First, the slight key backlash causes a slight distortion in the torque sensor waveform. Second, a higher frequency vibration

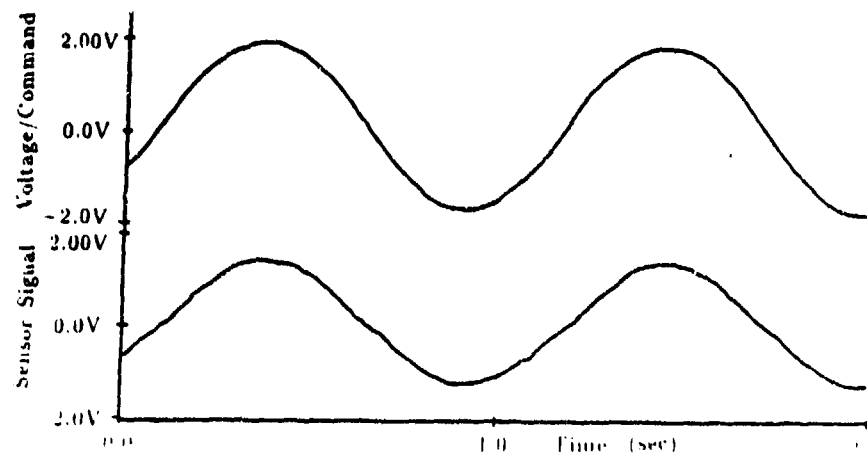


Figure 5.2 Joint torque sensor output with 1Hz sinusoidal input command provided to the motor.

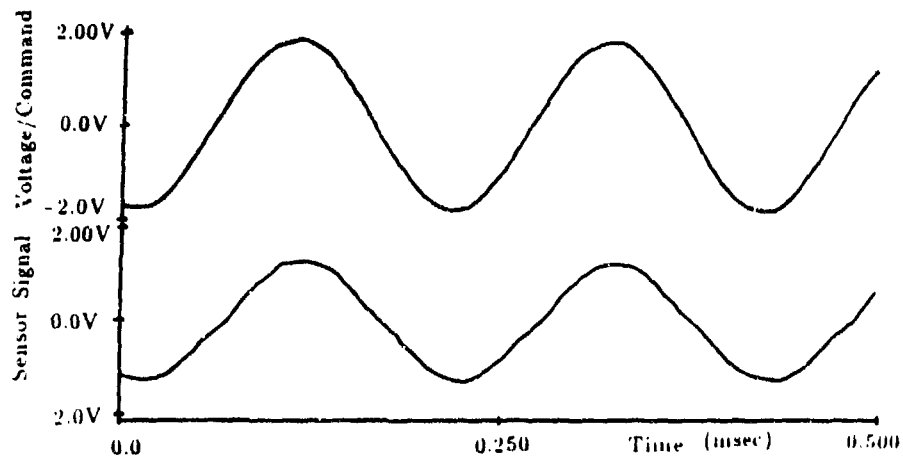


Figure 5.3 Joint torque sensor output with 5Hz sinusoidal input command provided to the motor.

mode appears in the output for the 25 and 50 Hz excitation frequencies.

Experiments were conducted to characterize the mode appearing in the excitation data and other significant dynamic modes. Initial calculations indicated that the motor rotor/torque sensor combination would exhibit two zeros (See Appendix III). The first zero would exist at ≈ 800 Hz and would involve the motor rotor and torque shaft inertia coupled with the sensor compliance. The second zero would appear at ≈ 2400 Hz and

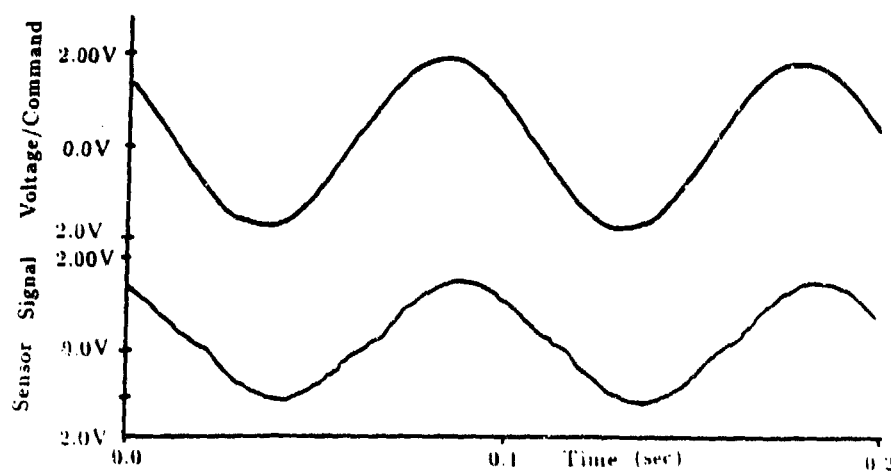


Figure 5.4 Joint torque sensor output with 10Hz sinusoidal input command provided to the motor.

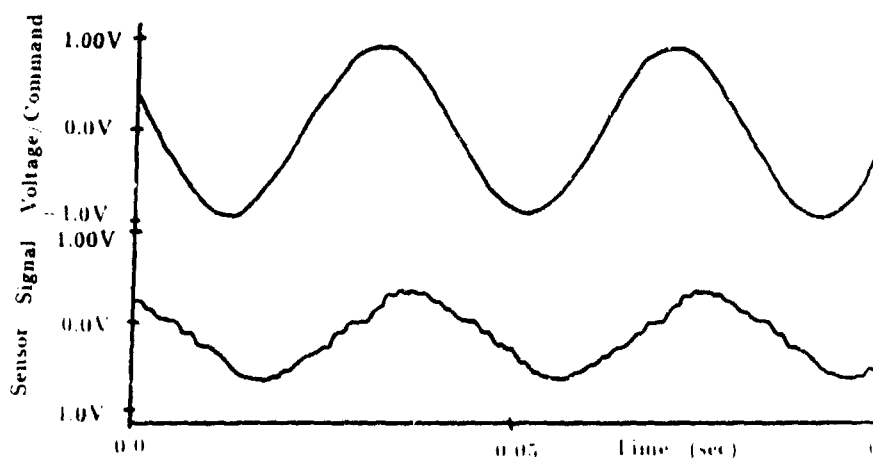


Figure 5.5 Joint torque sensor output with 25Hz sinusoidal input command provided to the motor.

involve the output pulley section supported by the sensor compliance.

The experiments consisted of exciting the zeroes in a pole configuration and recording the torque sensor output on an HP Logic Analyzer. In the case of the first calculated zero, the pulley was locked and the motor was given a step input. Figure 5.7 shows the resulting output of the torque sensor. A schematic of the physical situation is shown in Figure 5.8. The data indicates that the associated sensor/rotor zero is located at

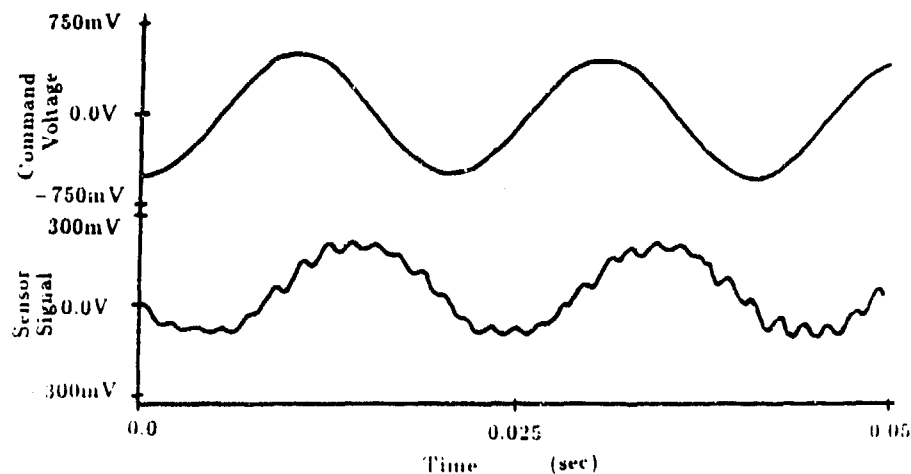


Figure 5.6 Joint torque sensor output with 50Hz sinusoidal input command provided to the motor.

≈ 600 Hz. Settling time is approximately 45 msec. It is this vibration mode which is superimposed on the frequency responses in Figure 5.7 and 5.8.

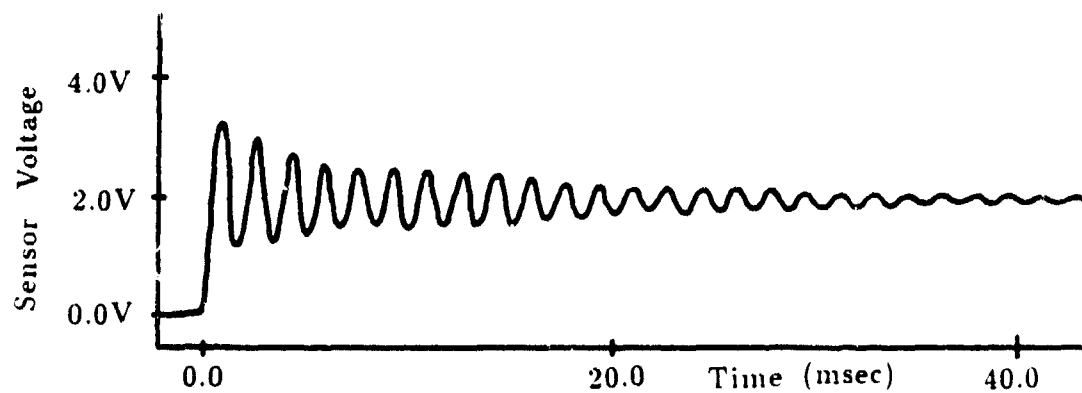


Figure 5.7 Sensor output from a step input command to the motor with the sensor pulley locked. The frequency is ≈ 600 Hz.

In order to identify the second zero, the motor shaft was locked and an impulse loading was applied to the sensor pulley. The resulting torque sensor output is presented in Figure 5.9. The physical situation is illustrated in Figure 5.10. The data indicates that the associated zero is located at ≈ 2600 Hz. The settling time is 4 msec.

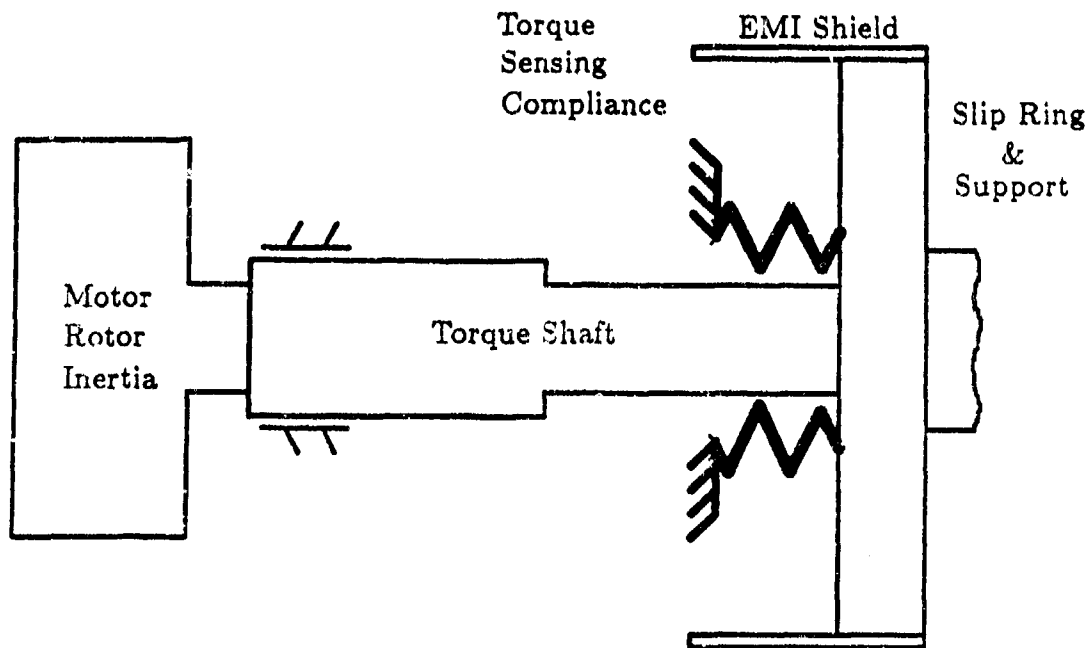


Figure 5.8 Schematic of the components contributing to the 600 Hz sensor zero.

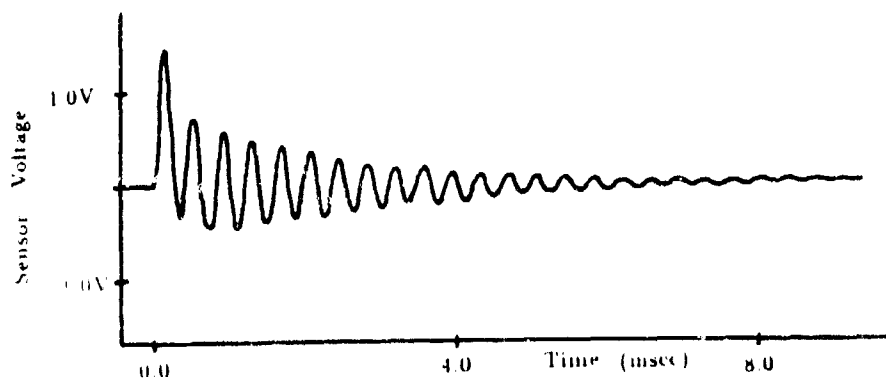


Figure 5.9 Sensor Output for an impulse loading of the sensor pulley with the motor shaft locked. The frequency is ≈ 2600 Hz.

These modes are high enough in frequency so that incorporation of the sensor into the lab's cable driven manipulator, should not adversely affect bandwidth. It is interesting to note that Figures 5.7 and 5.9 clearly show that the joint torque sensor

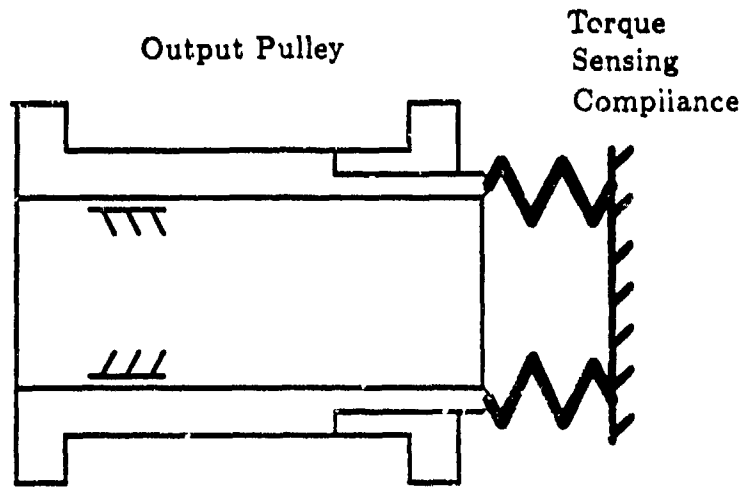


Figure 5.10 Schematic of the components contributing to the ≈ 2600 Hz sensor zero.

is not critically damped. Atkeson (1986) recommended that critical damping should be built into force sensors in the same way that accelerometers are critically damped. Atkeson felt that such damping might be appropriate in applications of closed loop force control. Unfortunately, initial experiments failed to provide a simple method of controlling sensor damping. Instead, the settling times of the important modes are presented to allow for proper accommodation in controller design.

5.2 Current Based Torque Control Results

Figure 5.11 presents the torque output of the Moog motor and controller as a function of commanded torque. No attempt was made to compensate for the deadband nonlinearity located around zero. It was felt that this problem would be best addressed through improved controller hardware (i.e. current sensors, etc.) or torque command modifica-

tion. It is important to note that much of this work was carried out in anticipation of receiving new and improved controller hardware from Moog. The new hardware, which will have been shipped by the time that this thesis goes to print, should improve several aspects of system performance including: current loop deadband, overall controller deadband (shown in Figure 5.11), and system stability. The work in this thesis has been aimed at improving motor/controller performance in other areas. From a systems standpoint, improvements in hardware, software, and our overall understanding of the system will eventually be combined to achieve an optimized torque control system.

The first attempt at current base torque control involved producing a lookup table of the effective motor torque constant as a function of shaft angle. This was accomplished by measuring output torque as a function of motor angle with the cantilever torque sensor. This data was then used to create a table of torque correction ratios which could be used to modify the torque commands before they were sent to the torque controller. This approach, implemented with a Vax 11/750, produced limited improvements in torque ripple ($\approx 50\%$). The success of the technique was limited by: 1) noise in the cantilever sensor torque measurements, and 2) transient variation in the phase angle of various torque ripple components.

The next approach involved closing a torque control loop and recording the phase currents necessary to produce linear torque output. The cantilever sensor, with improved cable shielding and the three stage low pass filter, was used to measure torque and a digital control loop was closed with the Vax 11/750. During the torque control,

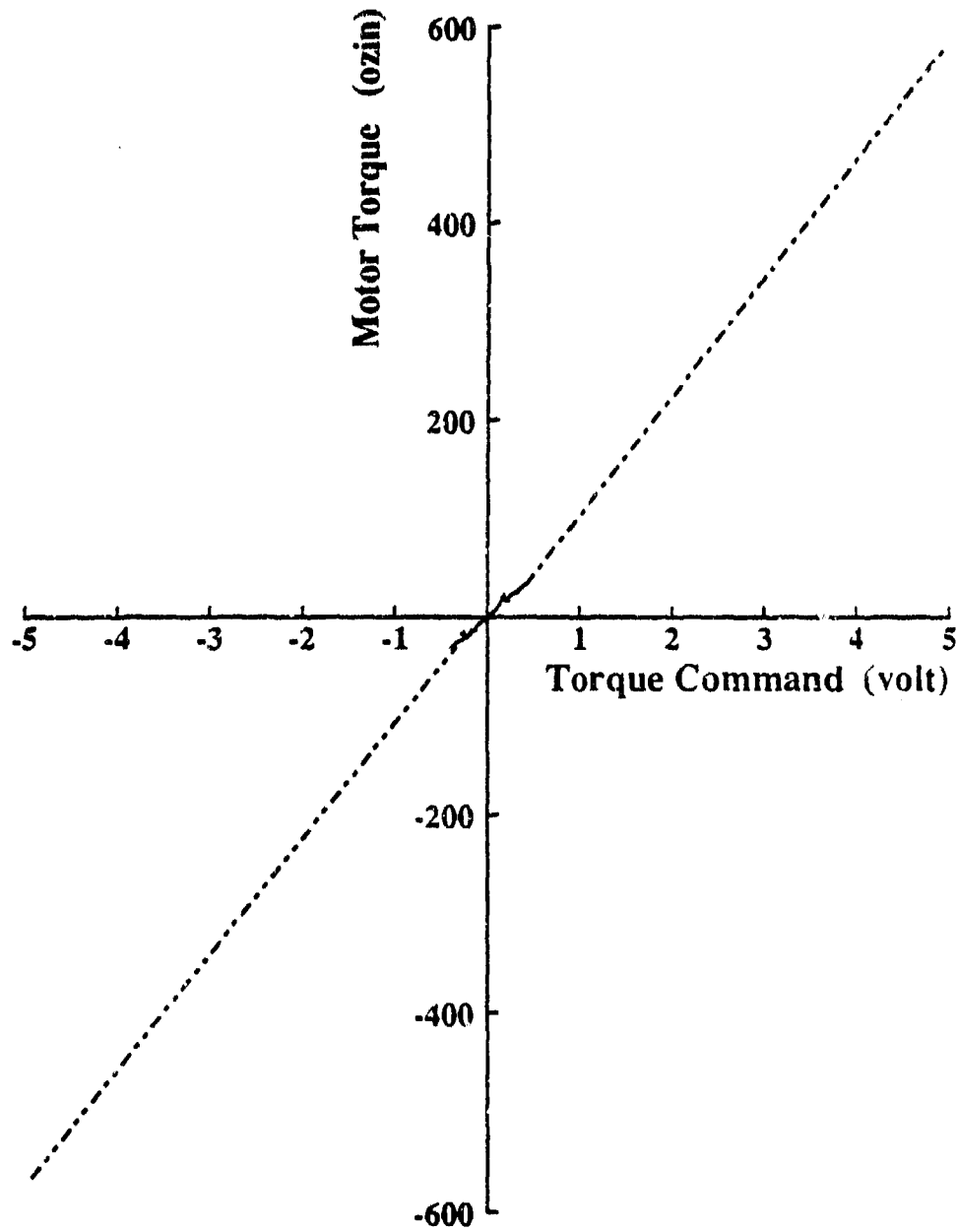


Figure 5.11 The calibration curve for the Moog controller.

the Vax was also used to read phase current command levels off the MDAC chips in the torque controller. Multiple readings were taken at each motor position as determined by the output of the resolver to digital converter in the motor controller. The recorded data was used to create new current waveform PROM tables. The results were interesting.

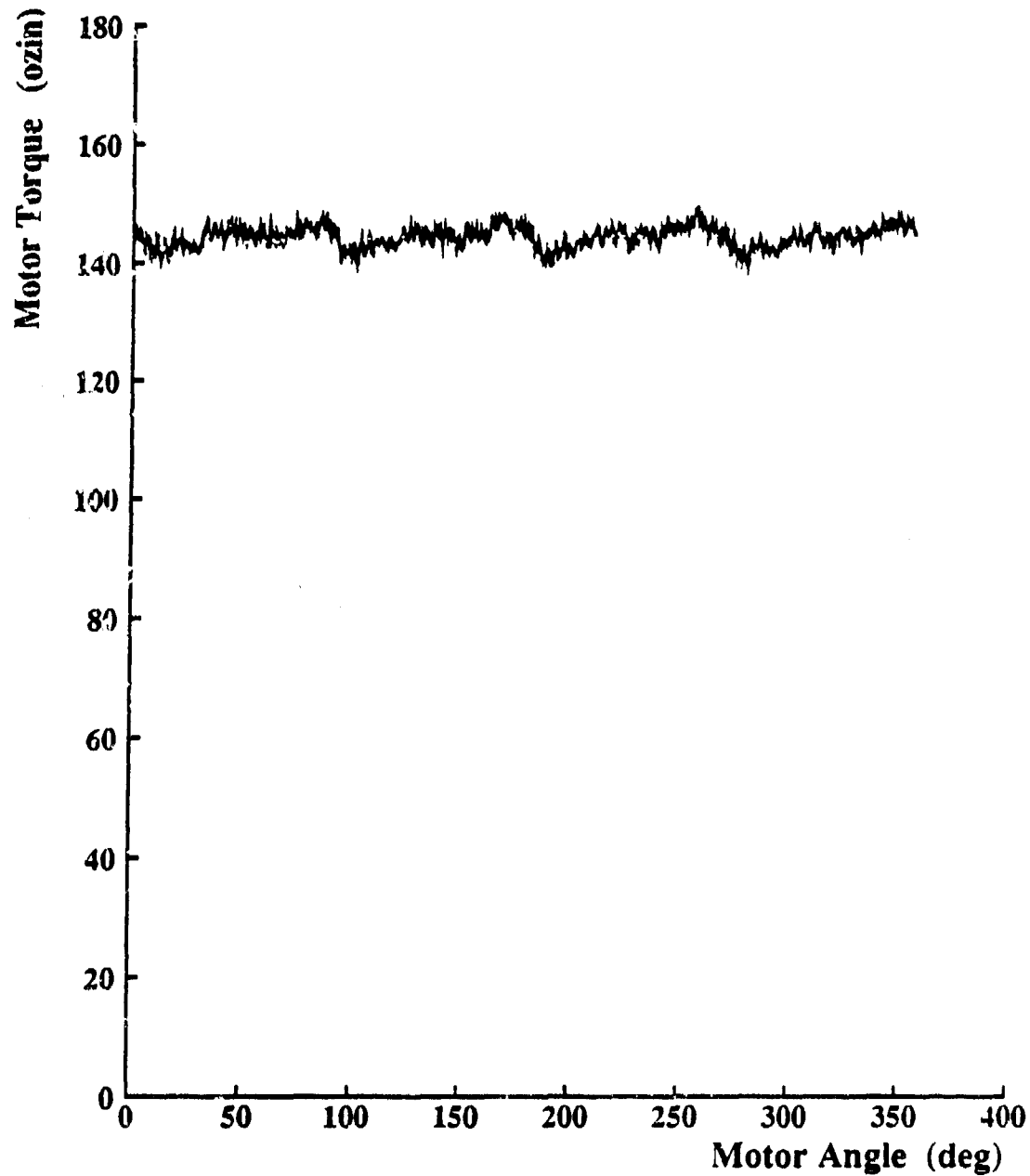


Figure 5.12 Torque compensated with the torque-loop-closure phase calibration method.

Overall torque ripple was reduced to $\approx \pm 2\%$ of output torque. Unfortunately, the results were transient. It is theorized that the torque performance based on PROM tables corrected in this way is particularly sensitive to changes in the actual motor

torque ripple. This is because the unstable and stable nonlinear torque characteristics are both an integral part of the actual correction. Therefore, while this technique offers temporary effectiveness, significant torque ripple returns to the output as the underlying motor/controller characteristics change. Figure 5.12 illustrates the initial torque performance improvement resulting from this technique.

Finally, feedforward torque compensation, based on an analysis of uncompensated output torque, was implemented on the Moog equipment. Figure 5.13 presents the resulting torque output as a function of shaft angle. The total torque variation is reduced from an uncompensated value of $\approx \pm 12\%$ to $\approx \pm 1.5\%$. The remaining variation is attributed to deadband and other nonlinearities. One advantage is that this technique is much less sensitive to transient effects in the controller and the resultant degradation of performance over time. In addition, the technique promises to produce excellent performance when it is implemented on the improved controller hardware. The results of each aspect of the feedforward compensation technique is presented in the following paragraphs.

The most significant torque ripple component in the Moog motor existed at twice the fundamental frequency and possessed a magnitude proportional to the torque command. It was theorized that this output ripple could be attributed to magnitude offsets in the fundamental phase current waveforms. As stated in Chapter 5, by carefully superimposing $n\theta_s$ sinewaves on the fundamental waveforms, one can generate $2n\theta$ compensating torque ripples of a desired phase and magnitude. Such an approach

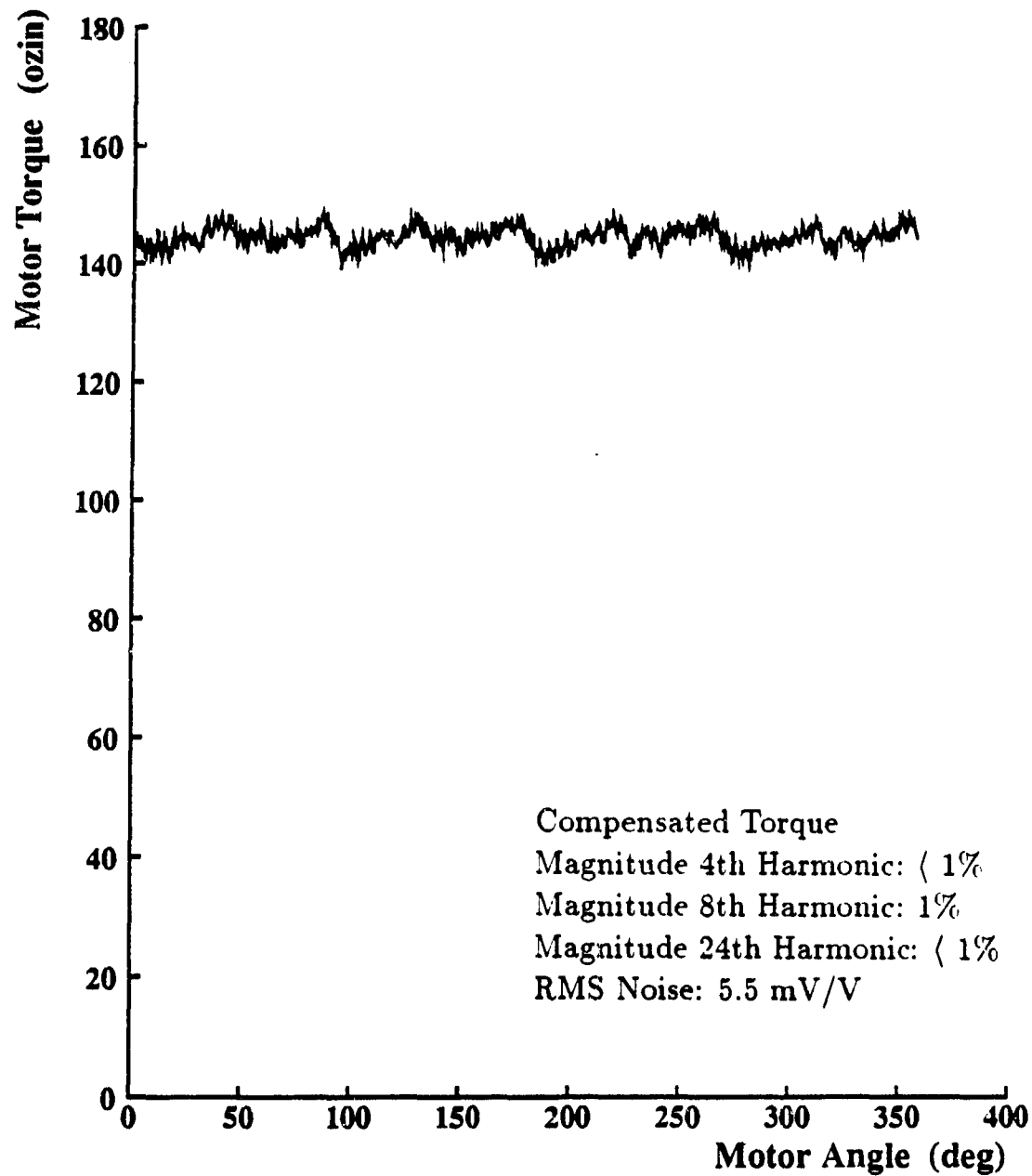


Figure 5.13 Torque compensated with commutation waveform modification based on output torque analysis.

was utilized with good results.

In order to compensate for an $\approx \pm 8\%$ ripple, a $12\% n\theta_6$ waveform was added to phase A, effectively increasing the phase A current magnitude. In order to compensate

for an 8θ ripple at 30° , it was necessary to draw this additional current through phase C. In light of this, the phase B waveform was not altered. The technique resulted in a reduction of the 8θ ripple to $\approx 1\%$ of output torque. Unfortunately, the remaining 8θ ripple component was not readily characterizable and therefore could not be compensated.

Torque ripple resulting from offsets in the fundamental current waveforms produced a constant $n\theta$ ripple of approximately $\pm 3\%$ of continuous output torque. Initially, the 4θ ripple was removed for given torque output levels by modifying the phase current lookup tables. This method was useful for analyzing the torque ripple and its correctability. Unfortunately, correction implemented in this way is proportional to output torque. Therefore, final compensation was achieved by adjusting zeroing pots in the phase current loop reference circuitry. This is clearly where the problem arises and therefore where it should be corrected from a systems standpoint. The end result was a 4θ ripple of approximately 0.5% of continuous output torque.

Torque ripple arising from motor spacial harmonics was minimized by entering corresponding current harmonics in the phase waveform tables. In order to accomplish this, the spacial harmonics were first identified. Figure 5.14 shows the results of torque measurements resulting when static current vectors were fed into the motor phases. Accuracy was increased by disconnecting the unused phase in each of the three experiments. In the first, a constant current was driven into phase C and out phase A. In the second, a constant current was driven into phase B and out phase C. The final

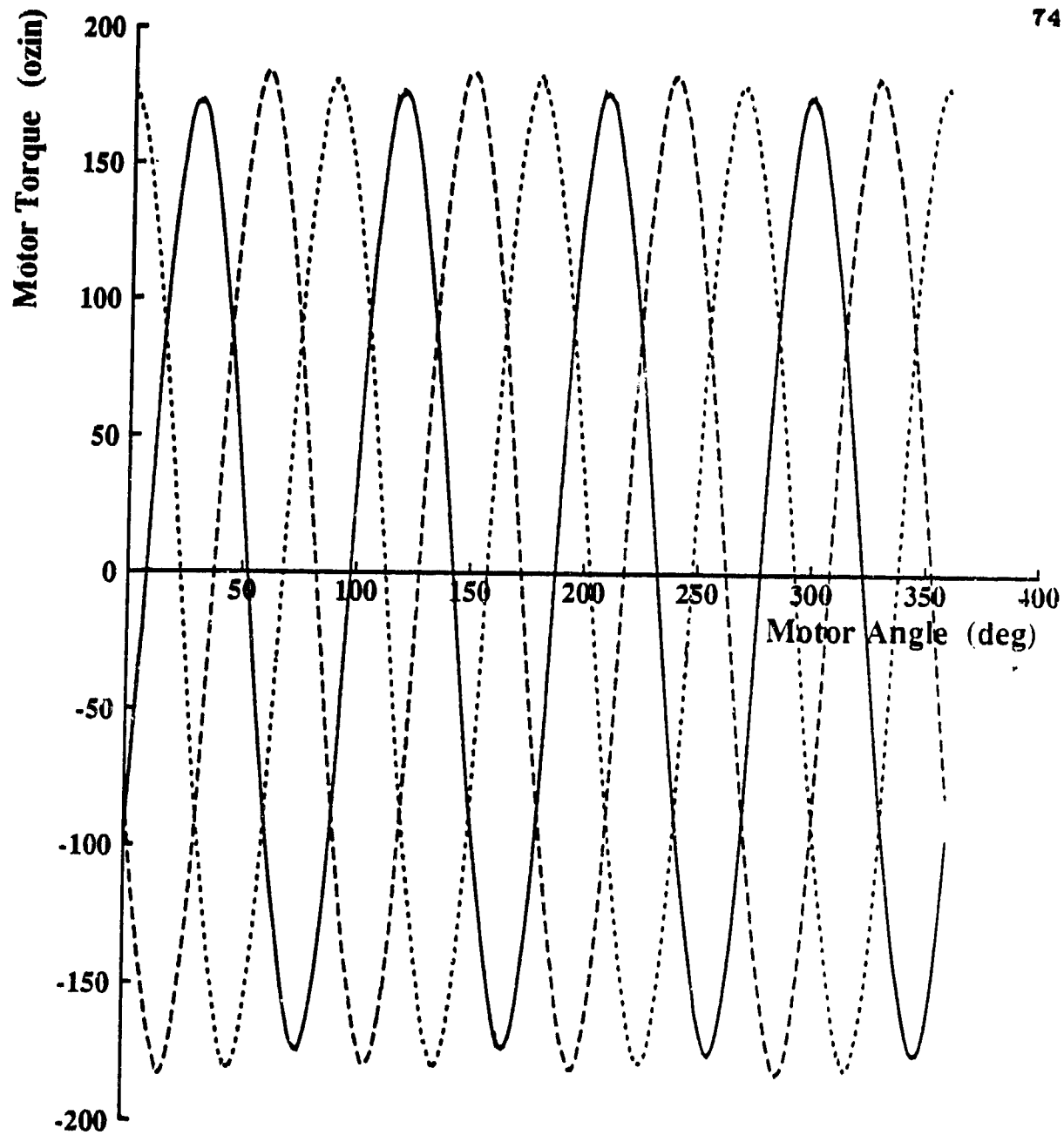


Figure 5.14 Harmonic identification output torques. The three curves are: dashed - phase A and C carrying current, dotted - phase B and C carrying current, and solid - phase A and B carrying current.

experiment involved driving a constant current into phase A and out phase B.

By performing an FFT on the data from each experiment, the significant spacial harmonics were identified and are shown in Figure 5.15. The magnitudes of the 5th and 7th harmonics are exaggerated relative to the primary frequency for clarity. The actual

magnitudes, normalized in relation to the fundamental spacial harmonic magnitude, were determined to be 0.008 for the 5th harmonic and -0.0017 for the 7th harmonic.

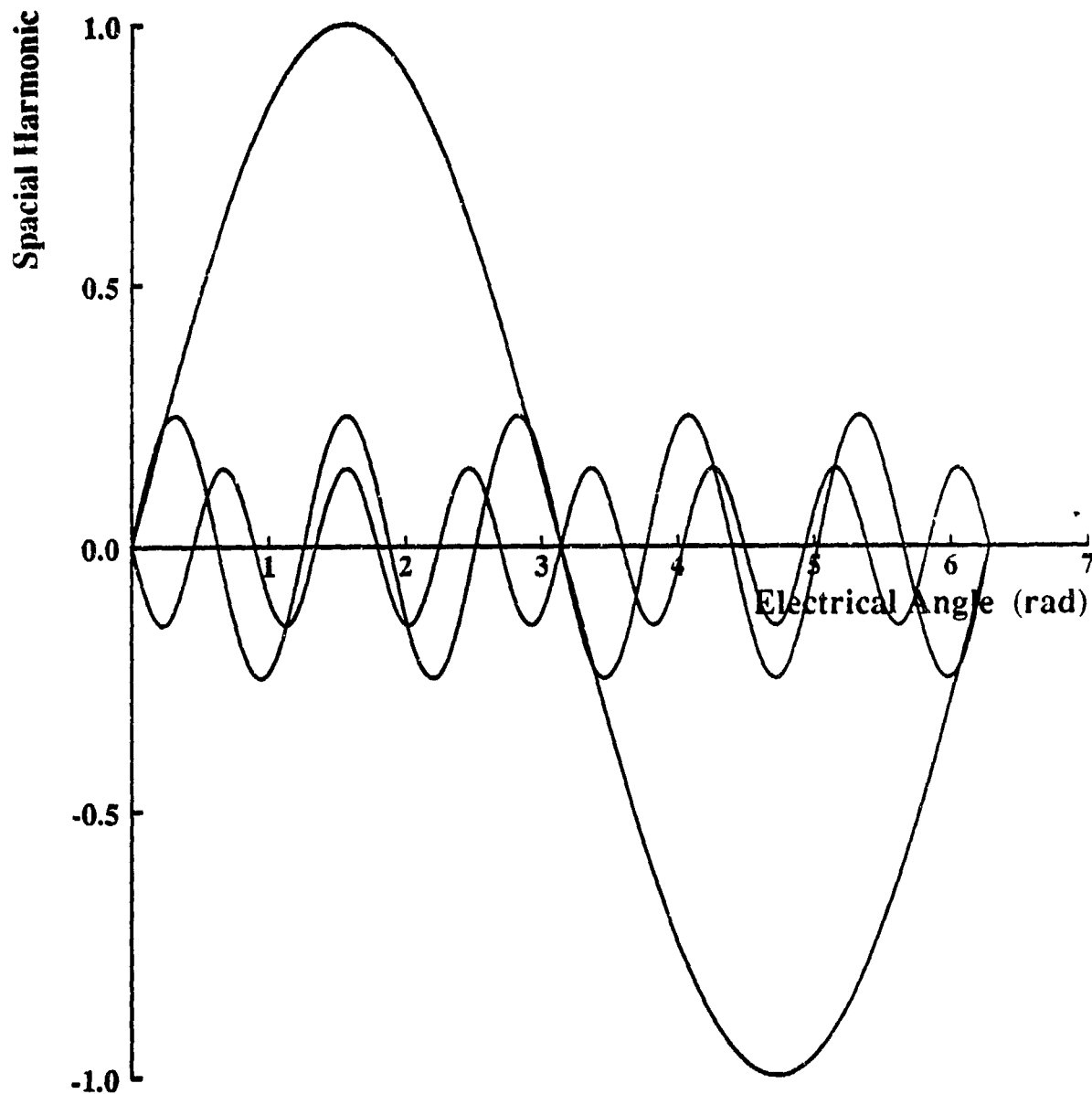


Figure 5.15 A componentwise decomposition of the motor spacial harmonics. The magnitudes of the 5th and 7th harmonics of the fundamental are exaggerated for clarity.

Compensation was accomplished by superimposing $5n\theta$ and $7n\theta$ sinusoids on the fundamental phase waveforms in the PROMs. Torque ripple at $6n\theta$ was reduced fivefold from $\pm 1.8\%$ to $\pm 0.3\%$ of output torque. Figure 5.16 illustrates the torque ripple

attributable to unmodeled motor spacial harmonics. Figure 5.17 presents the results of utilizing the higher order current harmonics to reduce this ripple. The other significant ripples have been removed to reveal the involved frequencies more clearly.

The implementation of current based torque control has demonstrated that it can be significantly improved through feedforward compensation and fundamental waveform modification. Overall, it appears that brushless motor output torque can be controlled with a reasonable degree of accuracy through phase current control. Torque ripple as a function of angle can be reduced to $\pm \approx 1.5\%$. In addition, the torque output can be reasonably calibrated with respect to input command, a situation that will improve with the new controller hardware.

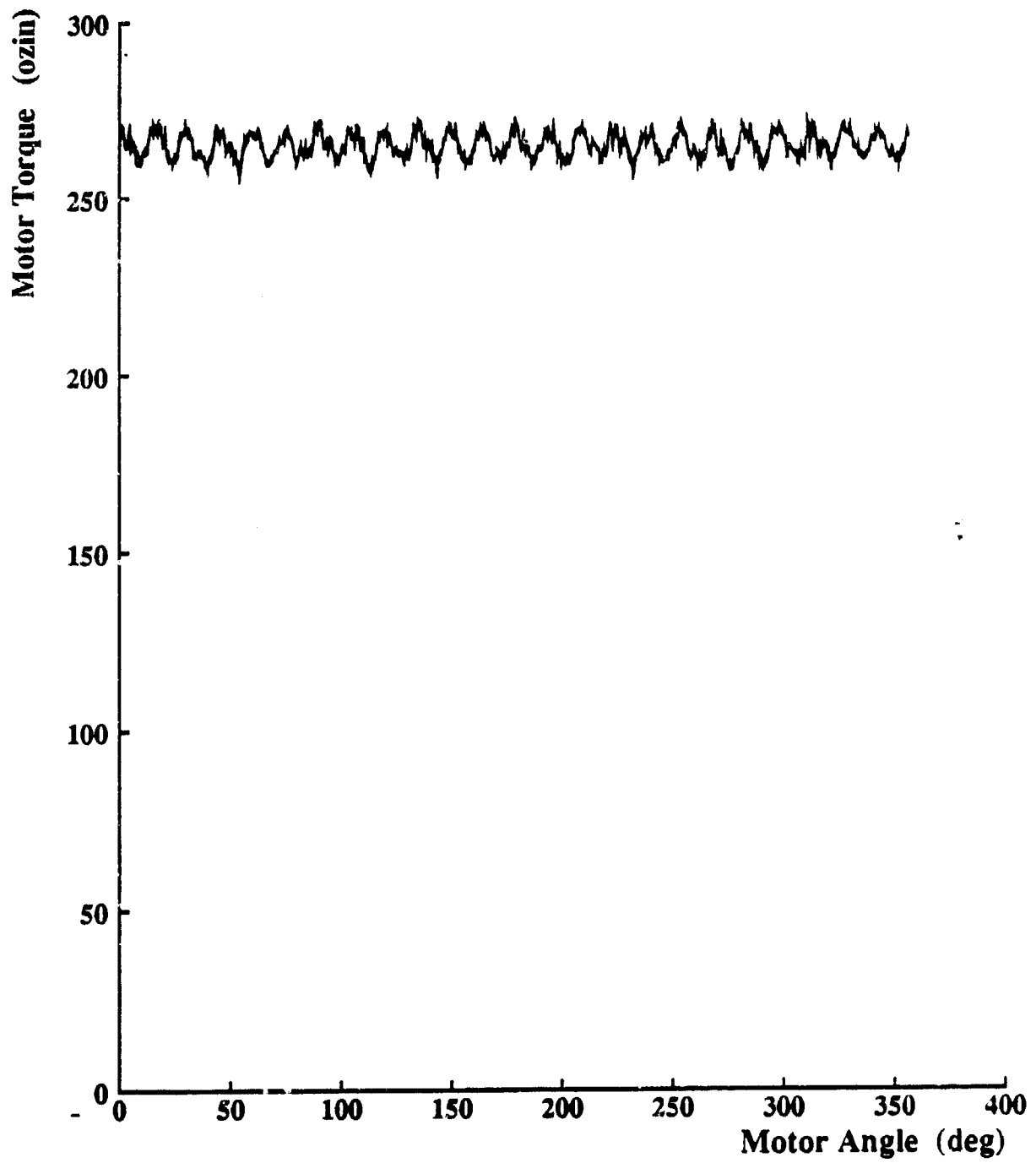


Figure 5.16 The Moog motor $6n\theta$ torque ripple component.

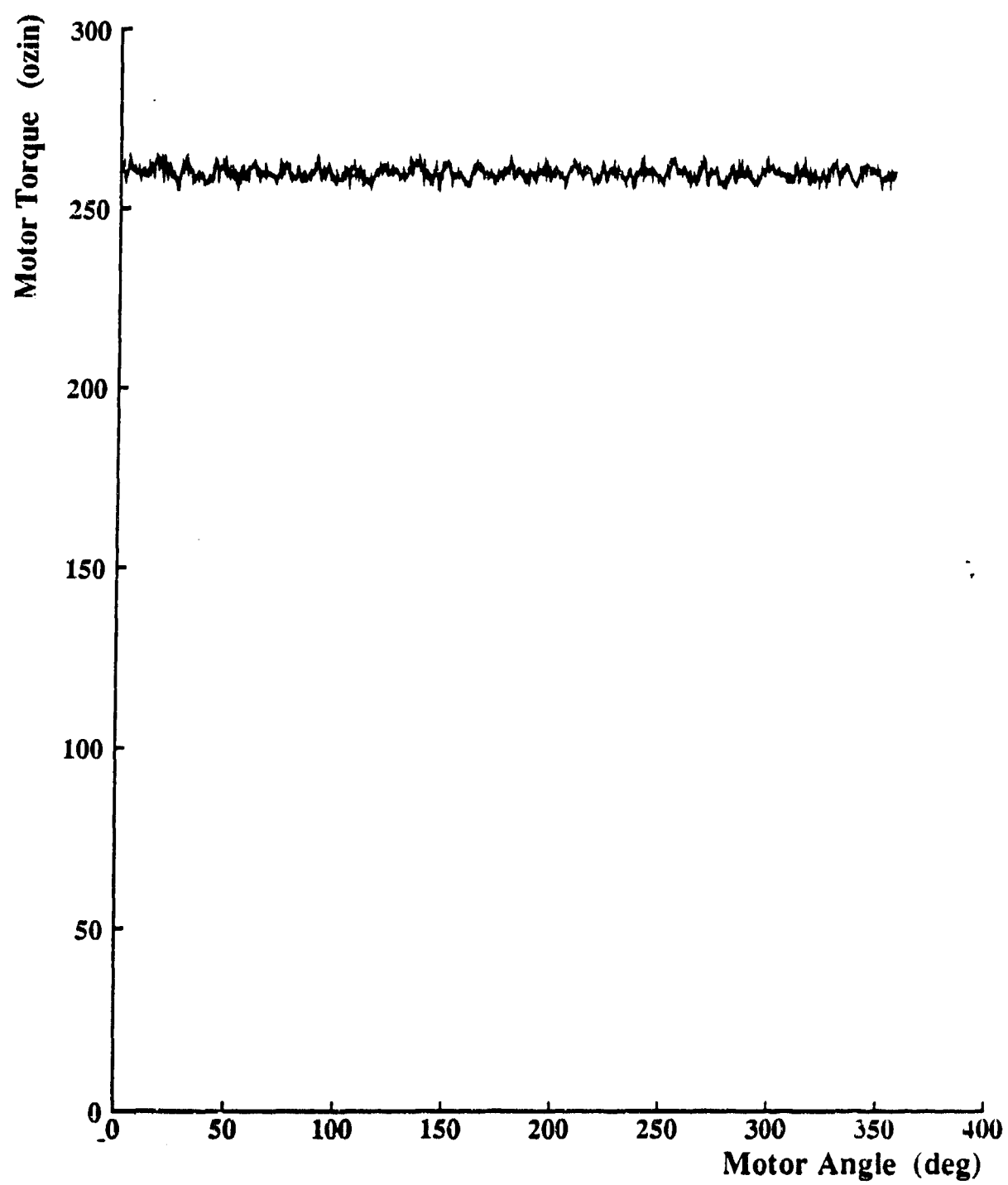


Figure 5.17 The Moog motor $6n\theta$ torque ripple component after harmonic compensation.

Chapter 6

Conclusion

Torque sensors were developed for torque measurement and feedback control of a Moog 303-003 brushless motor. The cantilever sensor provided a good instrument for recording torque output data. The joint torque sensor exhibits good linearity, repeatability, noise rejection, and dynamic characteristics. In addition, it is compatible with the current cable driven manipulator design being developed in the lab.

The torque characteristics of a Moog 303-003 brushless motor were studied. Output torque nonlinearities were identified and their origins were determined. Techniques were developed to compensate for torque nonlinearities through feedforward phase current compensation. It was found that the most significant sources of torque variation were: phase current offsets, phase current magnitude variations, current loop deadband, and unmodeled spacial harmonics. We feel that the best way to reduce the effect of these errors is to improve controller hardware and utilize phase waveform compensation techniques such as phase magnitude and spacial harmonic feedforward compensation.

Overall, it is apparent that the need for torque sensor feedback can no longer be assumed in the torque control of brushless motors. Current based torque control techniques can provide very reasonable accuracy levels with less complexity and higher bandwidth than is possible with torque sensors. Therefore, one must take a look at the

entire torque control system and decide what is the best torque control technique for a given application.

Appendix I

Moog Motor 303-003

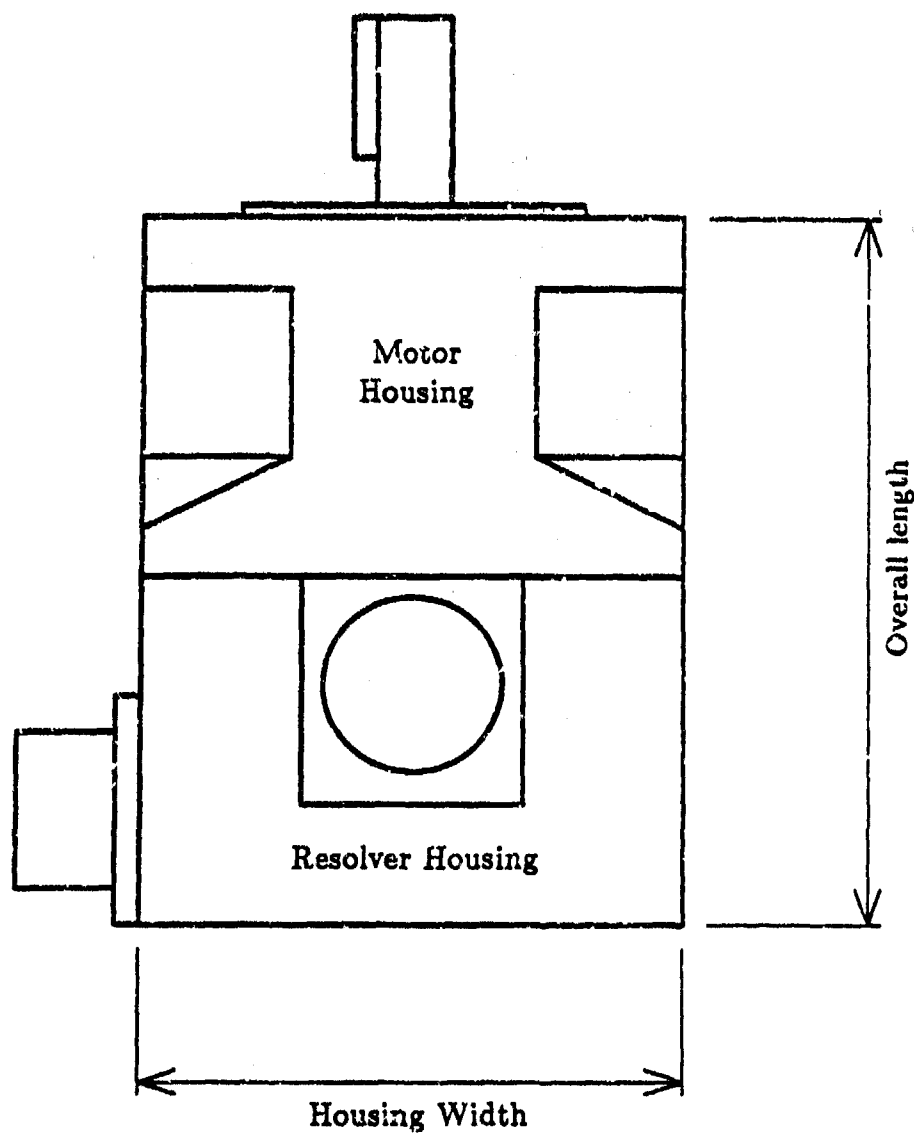
Performance Specification	English Units	Metric Units
Continuous Stall Torque	15 in.lb.	1.7 NM
Continuous Stall Current	7.6 Amps	7.6 Amps
Peak Stall Torque	60 in.lb.	6.8 NM
Peak Stall Current	26.9 Amps	26.9 Amps
Torque Constant	2.4 in.lb./A	0.27 NM/A
Voltage Constant	27.8 V/KRPM	0.27 V/rad/sec
Motor Constant	26.6 ozin/ \sqrt{watt}	0.19 NM/ \sqrt{watt}
Rotor Inertia	0.00036 in.lb.sec ²	0.000041 Kg ^m ²
Mechanical Time Constant	1.00 mS	1.00mS
Resistance Term/Term	1.8 Ohms@77°F	1.8 Ohms@25°C
Electrical Time Constant	1.72 mS	1.72 mS
Overall Weight	3.5 lb.	1.6 Kg
Length	4.66 in.	118.4 mm
Width	2.75 in.	69.9 mm
No Load Speed	11000 RPM	11000 RPM

Brushless Resolver

Performance Spec	Value
Input Voltage	6.0 VAC
Input Frequency	1000 Hz
Input Current Max	15.0 mA
Transformation Ratio	.45:1
Output Voltage	2.72 VAC

Moog Torq Controller 152-002

Performance Spec	Value
Continuous Current	15 Amps
Peak Current	30 Amps
Switching Frequency	5KHz
Efficiency	95%
Driver Voltage	325 Volt



Overall Length: 3.66 in.

Housing Width: 2.75 in.

Output Shaft: 0.375 in. dia.

Figure A.I.1. Moog 303-003 Brushless Motor and Resolver.

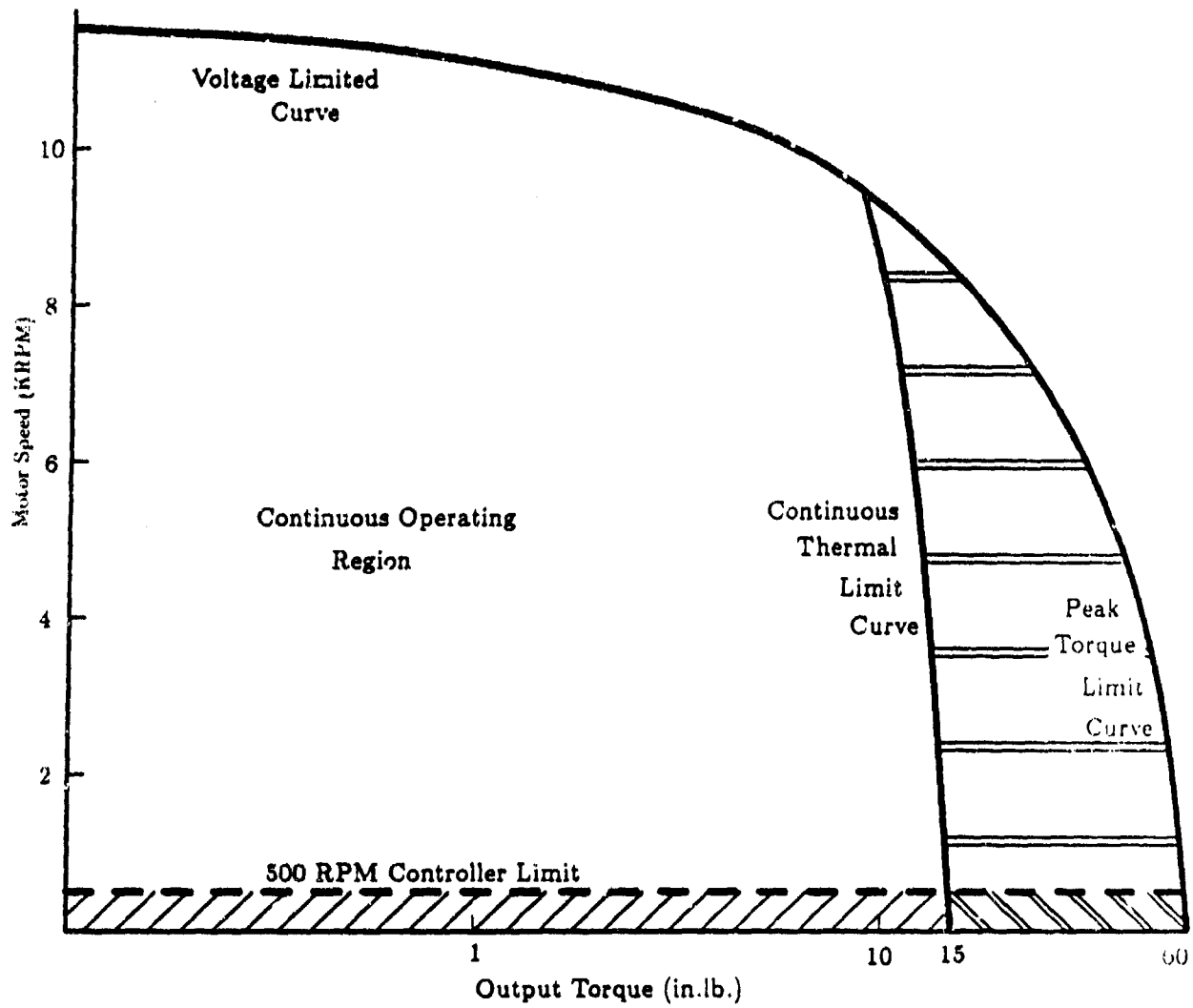


Figure A.1.2. Moog 303-003 Performance Curve.

Appendix II

The Design of a Cantilever Torque Sensor

The cantilever beam shown in Figure A.2.1 has the following characteristics:

$$b = 0.340\text{in.}$$

$$h = 0.240\text{in.}$$

$$d1 = 0.700\text{in.}$$

$$d2 = 1.700\text{in.}$$

$$E = 10^6 \text{psi}$$

The strain at the gauges under maximum torque loading is calculated using standard equations:

$$I = \frac{1}{12}bh^3 = \frac{1}{12}(.34\text{in.})(.24\text{in.})^3$$

$$M = \tau \frac{(d2 - d1)}{d2} = (60\text{in. lb.}) \frac{(1.7\text{in.} - 0.7\text{in.})}{1.7\text{in.}} = 35.294\text{in. lb.}$$

where D1, D2, b, and h are shown in Figure A.2.1. The stress is computed from:

$$\text{Stress} = \frac{Mc}{I} = \frac{6M}{bh^2} = \frac{6(35.3\text{in. lb.})}{(.34\text{in.})(.24\text{in.})^2} = 10,813 \frac{\text{lb.}}{\text{in.}^2}$$

Which allows the gauge strain to be calculated:

$$\text{Strain} = \frac{\text{Stress}}{E} = \frac{10,813\text{psi}}{10^6\text{psi}} \approx 1100\mu\text{in/in}$$

The gauge electronics are shown in figure A.2.2. The following characteristics are

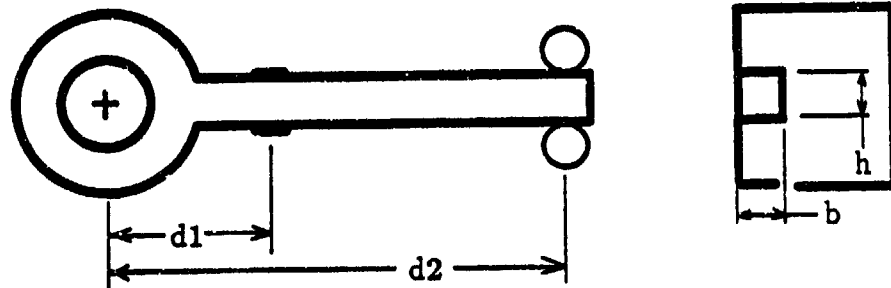


Figure A.2.1 The aluminum cantilever beam and relative positioning of the strain gauges and dowel pin stops.

noted:

$$\text{Gauge Resistance} = 350\Omega$$

$$G = \text{Gauge Factor} = \frac{\text{Change in Resistance}}{\text{Strain}} = 135\Omega$$

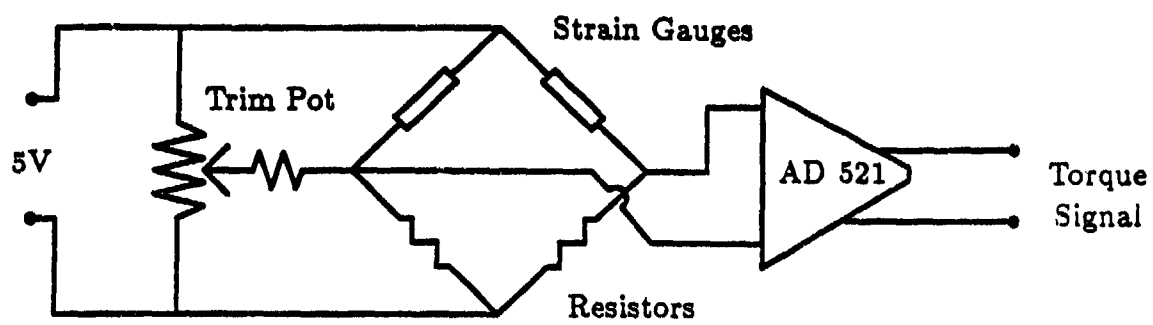
$$E_b = 5\text{volts}$$

The necessary gain is calculated as follows:

$$\Delta R = GR(\text{Strain})$$

$$E_0 = E_b \left(\frac{R_1}{(R_1 + R_4)} - \frac{R_2}{(R_2 + R_3)} \right) = 0.359\text{volts}$$

$$\text{Amplifier Gain} = \frac{10\text{volts}}{0.359\text{volts}} = 28$$



Wheatstone Half Bridge

Figure A.2.2 An electrical schematic for the cantilevered sensor electronics.

Appendix III

The Design Equations for the Joint Torque Sensor

The gauging surface was designed to withstand reasonable loadings and provide 1000 μ in./in. strain at the strain gauge orientation under peak torque loading conditions. The strain gauges were oriented at 45° and 135° to the shaft axis in order to measure maximum normal strain arising from torsional loading. The following equation gives the 45° strain under torsional loading for a thin walled tube:

$$Strain_{45^\circ} = \frac{(Torque)R_o}{\pi G(R_o^4 - R_i^4)}$$

The I.D. for the gauging surface was chosen to be 0.5432 in. This diameter corresponds to a 17/32 in. standard reamer and was chosen for manufacturability.

$$Strain_{45^\circ} = \frac{(60in.lb.)(0.2716in.)}{\pi(11.5e^6psi)(0.2716^4 - 0.2656^4)}$$

$$Strain_{45^\circ} = 970\mu in./in.$$

The stiffness of the sensor is calculated based on the following equation:

$$Stiffness = \frac{Torsional\ Moment}{Angular\ Deflection}$$

$$Stiffness = \frac{\pi G(R_o^4 - R_i^4)}{2l} = \frac{\pi(11.5e^6psi)(.2716^4 - .2656^4)}{2(.3383)}$$

$$Stiffness = 24,830 \frac{lb.in.}{rad} \approx 360(Cable\ Stiffness)$$

Torsional Buckling Stress

Check for buckling (Roark and Young (1983)) due to torsion:

$$\frac{\tau}{t} = \frac{0.2716}{0.006} = 45$$

Since this is greater than 10, the following equations apply and the actual shear stress and approximate buckling torsional stress can be calculated.

$$\text{Shear Stress} = \frac{T}{2\pi r^2 t} = \frac{60 \text{ in. lb.}}{2\pi (0.2716)^2 (0.006)}$$

$$\text{Buckling Stress} \approx 18 \text{ ksi}$$

$$\text{Buckling Stress} = \frac{0.60E t^2}{1 - \mu^2 l} (-2.39 + \sqrt{96.9 + 0.605H^{1.5}})$$

where $\mu = 0.28$ and:

$$H = \sqrt{1 - \mu^2} \left(\frac{l^2}{tr} \right)$$

$$H = \sqrt{1 - .28^2} \frac{0.3383^2}{(0.006(0.2716)^2)} \approx 67$$

$$\text{Buckling Stress} \approx 112 \text{ ksi}$$

Check the factor of safety:

$$\text{Factor of Safety} = \frac{\text{Buckling Stress}}{\text{Shear Stress}} = \frac{112 \text{ ksi}}{18 \text{ ksi}} \approx 6$$

Axial Buckling Stress

Check for buckling (Roark and Young (1983)) due to axial loading:

$$\text{Buckling Stress} \approx \frac{0.40}{\sqrt{3}} \frac{E}{\sqrt{1 - \mu^2}} \frac{t}{r} = \frac{0.40}{\sqrt{3}} \frac{30e^6}{\sqrt{1 - .28^2}} \frac{0.006}{0.273}$$

$$\text{Buckling Stress} \approx 160 \text{ ksi}$$

The maximum end loading can now be calculated:

$$\text{Section Area} \approx 0.006\text{in}(2\pi)0.275\text{in} \approx 0.01\text{in}^2$$

$$\text{Maximum Thrust Load} = \text{Buckling Stress}(\text{Area}) \approx 1600\text{lb.}$$

Strain Gauge Calculations

The surface strain at the orientation of the strain gauges is calculated for the gauge section:

$$\text{Strain}_{45^\circ} = \frac{Mr_o}{\pi G(r_o^4 - r_i^4)} = \frac{60\text{inlb}(0.5432/2)}{\pi(11.5e^6)((0.5432/2)^4 - (0.5312/2)^4)}$$

$$\text{Strain}_{45^\circ} \approx 1000\mu\text{in/in}$$

Amplifier Gain

Calculate the change in resistance for peak strain:

$$\Delta R = GR(\text{Strain})$$

Given that $G = \text{Gauge Factor} = 120$, $\Delta R = 34\Omega$, for a full Wheatstone Bridge:

$$E_g = E_0 \left(\frac{R_1}{R_1 + R_4} - \frac{R_2}{R_2 + R_3} \right) = 5.0V \left(\frac{384}{384 + 316} - \frac{316}{316 + 384} \right) = 0.58V$$

This value is $\approx 9.6\text{mV/in.lbf}$. The actual value was 8.9mV/in.lbf . and therefore the gain was set to 22. This was done in order to produce a full scale signal of $\pm 12V$ at peak torque.

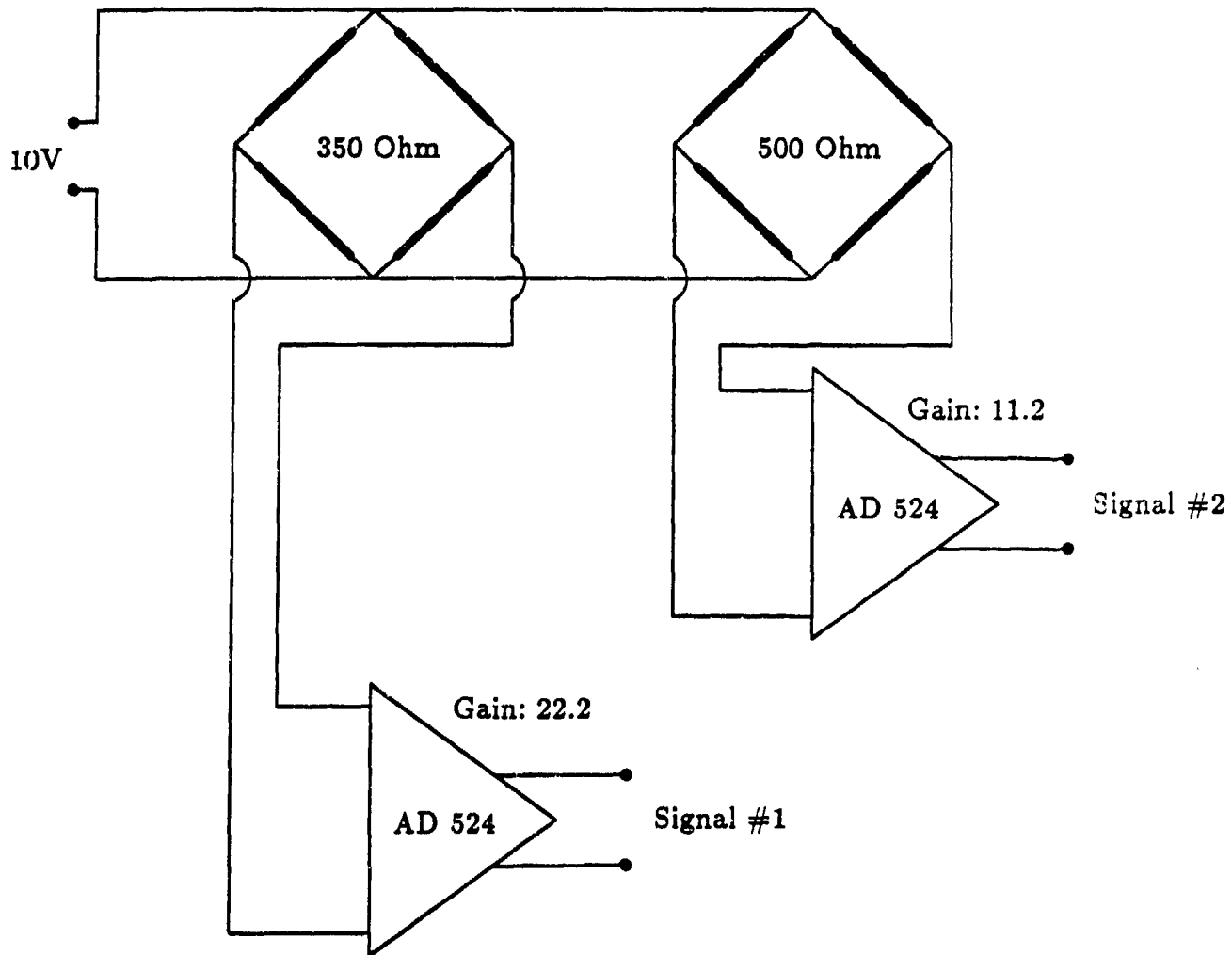


Figure A.3.1 An electrical schematic for the joint torque sensor electronics.

Vibrational Modes

Calculate the zeroes of the torque sensor:

$$\text{Stiffness} = 24,830 \text{ lb/rad}$$

Roughly calculate the pulley section inertia:

$$I = \frac{d w \pi r^4}{2} = \frac{(0.5 \text{ lb/in}^3)(1.5 \text{ in})(\pi)(0.6 \text{ in})^4}{(2)(32.2 \text{ lbf/lbm ftsec}^2)(12 \text{ in/lb})}$$

$$Inertia = 0.000114 \text{ lb fin sec}^2$$

$$\omega_n = \sqrt{\frac{k}{I}} = \sqrt{\frac{24830 \text{ lb fin sec}^2}{0.000114 \text{ in lb fin sec}^2}} \approx 14770 \text{ rad/sec}$$

$$\omega_n = 2350 \text{ Hz}$$

Look at the other zero:

$$I = \frac{(0.3 \text{ lb fin}^2)(0.25 \text{ in})(\pi)(1 \text{ in})^4}{(2)(32.2 \text{ lb fin}^2/\text{lb fin ft sec}^2)(12 \text{ in}/\text{lb})} = 0.000305 \text{ lb fin sec}^2$$

$$I_{slipring} \approx 0.000223 \text{ lb fin sec}^2$$

$$I_{motor \text{ rotor}} \approx 0.000360 \text{ lb fin sec}^2$$

$$I_t = I + I_{slipring} + I_{motor \text{ rotor}} = 0.000888 \text{ lb fin sec}^2$$

$$\omega_n = \sqrt{\frac{K}{I_t}} = \sqrt{\frac{24,830 \text{ lb fin/rad}}{0.000888 \text{ lb fin sec}^2}} = 5288 \text{ rad/sec}$$

$$\omega_n \approx 840 \text{ Hz}$$

References

Abramowitz, J.D., "Force Control of Robotic Manipulators", Artificial Intelligence Lab, Massachusetts Institute of Technology, Jan., 1984.

Aha, Eugene, "DC Motors and Generators", *Motion*, pp.3-12., January/February, 1987.

An, C.H., "Trajectory and Force Control of a Direct Drive Arm". PhD Thesis. Massachusetts Institute of Technology, 1986.

Asada, H., Lim, S-K., "Design of Joint Torque Sensors and Torque Feedback Control for Direct-Drive Arms", *ASME Winter Annual Meeting*, pp. 277-284. Nov. 17-22, 1985.

Asada, H. and Youcef-Tourni, K., "Development of a Direct-Drive Arm Using High Torque Brushless Motors", Laboratory for Manufacturing and Productivity. Massachusetts Institute of Technology.

Asada, H., Youcef-Toumi, K. *Direct-Drive Robots Theory and Practice*. MIT Press: Cambridge, MA., 1987.

Asada, H., Youcef-Toumi, K., and Lim, S.K., "Joint Torque Measurement of a Direct-Drive Arm", *23d IEEE Conference on Decision and Control*. pp. 1332-1337. Dec., 1984.

Atkeson, Christopher Granger, "Roles of Knowledge in Motor Learning". PhD Thesis, Massachusetts Institute of Technology, 1986.

Cannon, R.H. and Rosenthal, D.E., "Experiments in Control of Flexible Structures with Noncollocated Sensors and Actuators", *AIAA Journal of Guidance and Control*. Vol. 3, No. 3, pp. 546-553, Sept.-Oct., 1984.

Cannon, R.H. and Schmitz, E., "Initial Experiments on the End-Point Control of a Flexible One-Link Robot", *The International Journal of Robotics Research*, Vol. 3, No.3, pp. 62-75, Fall 1984.

Cannon, R.H., Tilley, S.W., and Kraft, Ray, "End Point Force Control of a Very Flexible Manipulator with a Fast End Effector". *ASME Winter Annual Meeting*. Anaheim, CA., Dec., 1986.